Cell Reports

Article

BRAF^{V600E} in colorectal cancer reduces sensitivity to oxidative stress and promotes site-specific metastasis by stimulating glutathione synthesis

Graphical abstract

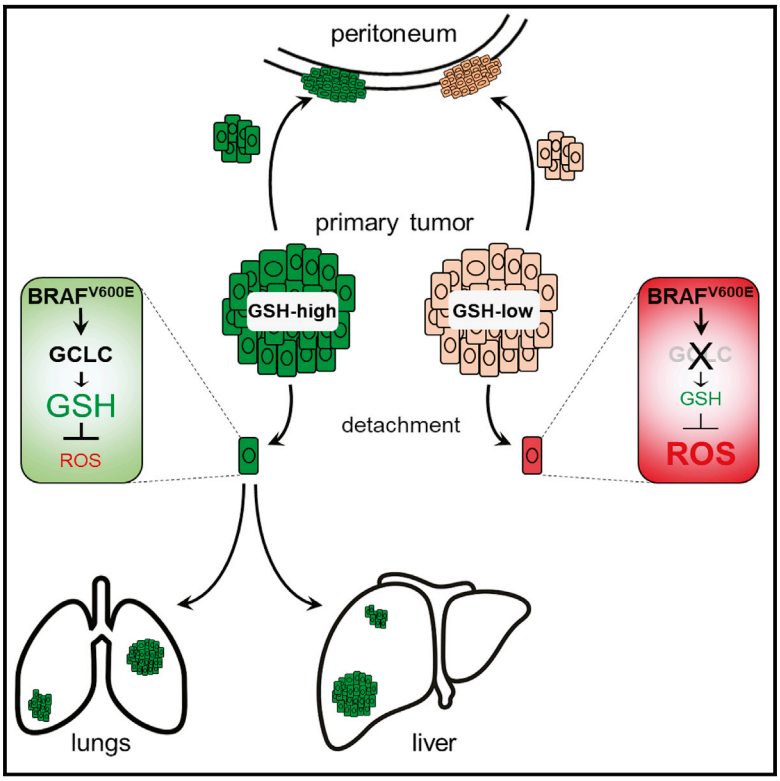

Highlights

- BRAF^{V600E} drives expression of glutamate-cysteine ligase (GCL) in colorectal cancer
- GCLC-mediated glutathione synthesis increases resistance to oxidative stress
- The BRAF^{V600E}-GCLC-glutathione pathway promotes liver and lung metastasis formation
- The pathway does not control formation of primary tumors or peritoneal metastases

Authors

Jamila Laoukili, Susanne van Schelven, Emre Küçükköse, ..., Miriam Koopman, Inne Borel Rinkes, Onno Kranenburg

Correspondence

j.laoukili@umcutrecht.nl (J.L.), o.kranenburg@umcutrecht.nl (O.K.)

In brief

The mechanisms governing distant metastasis formation in colorectal cancer are incompletely understood. Laoukili et al. show that the BRAF^{V600E} oncogene increases the capacity of disseminated tumor cells to withstand metastasis-associated oxidative stress by stimulating glutathione synthesis. This pathway promotes the formation of liver and lung metastases but not peritoneal metastases.

Laoukili et al., 2022, Cell Reports *41*, 111728
November 29, 2022
https://doi.org/10.1016/j.celrep.2022.111728

CellPress

Cell Reports

CellPress
OPEN ACCESS

Article

$BRAF^{V600E}$ in colorectal cancer reduces sensitivity to oxidative stress and promotes site-specific metastasis by stimulating glutathione synthesis

Jamila Laoukili,[1,*] Susanne van Schelven,[1] Emre Küçükköse,[1] André Verheem,[1] Kaitlyn Goey,[2] Miriam Koopman,[2] Inne Borel Rinkes,[1] and Onno Kranenburg[1,3,4,*]

[1]Lab Translational Oncology, University Medical Center Utrecht, G04-228, PO Box 85500, 3508GA Utrecht, the Netherlands
[2]Department of Medical Oncology, University Medical Center, Utrecht University, Utrecht, the Netherlands
[3]Utrecht Platform for Organoid Technology, Utrecht University, Utrecht, the Netherlands
[4]Lead contact
*Correspondence: j.laoukili@umcutrecht.nl (J.L.), o.kranenburg@umcutrecht.nl (O.K.)
https://doi.org/10.1016/j.celrep.2022.111728

SUMMARY

The presence of $BRAF^{V600E}$ in colorectal cancer (CRC) is associated with a higher chance of distant metastasis. Oxidative stress in disseminated tumor cells limits metastatic capacity. To study the relationship between $BRAF^{V600E}$, sensitivity to oxidative stress, and metastatic capacity in CRC, we use patient-derived organoids (PDOs) and tissue samples. $BRAF^{V600E}$ tumors and PDOs express high levels of glutamate-cysteine ligase (GCL), the rate-limiting enzyme in glutathione synthesis. Deletion of GCL in $BRAF^{V600E}$ PDOs strongly reduces their capacity to form distant liver and lung metastases but does not affect peritoneal metastasis outgrowth. Vice versa, the glutathione precursor N-acetyl-cysteine promotes organ-site-specific metastasis in the liver and the lungs but not in the peritoneum. $BRAF^{V600E}$ confers resistance to pharmacologically induced oxidative stress *in vitro*, which is partially overcome by treatment with the BRAF-inhibitor vemurafenib. We conclude that GCL-driven glutathione synthesis protects $BRAF^{V600E}$-expressing tumors from oxidative stress during distant metastasis to the liver and the lungs.

INTRODUCTION

Colorectal cancer (CRC) is a highly heterogeneous disease consisting of multiple genetic and molecular subtypes[1] and remains one of the prime causes of cancer-related mortality in the Western world.[2] One specific amino acid substitution in the *BRAF* proto-oncogene (V600E) causes constitutive activation of its kinase domain and accounts for more than 80% of the *BRAF* mutations in CRC.[3] Importantly, the presence of $BRAF^{V600E}$ in CRC is associated with an increased risk of mortality due to distant metastasis.[4] By contrast, non-V600 BRAF mutations are associated with a better survival in CRC, possibly relating to their lower impact on downstream activation of the MAPK pathway when compared with $BRAF^{V600E}$.[5–8]

The molecular underpinnings of the aggressive behavior of $BRAF^{V600E}$ CRC remain largely unclear.[9] An emerging theme in metastasis research is the notion that reactive oxygen species (ROS) play an important role during dissemination and metastatic colonization. Oncogenic transformation is generally associated with increased ROS production, which may contribute to establishment of the transformed phenotype.[10–14] However, ROS levels are further elevated following the detachment of tumor cells from neighboring cells[15,16] and from the extracellular matrix.[17] The resulting oxidative stress is an important barrier for metastasis formation.[15–24] The formation of liver metastases by CRC cells depends on glutathione (GSH)-mediated neutralization of oxidative stress.[18,21] The first and rate-limiting step of GSH biosynthesis is catalyzed by glutamate-cysteine ligase (GCL).[25] GSH neutralizes H_2O_2 and other peroxides via the action of GSH peroxidases (GPXs), and it detoxifies harmful electrophiles through GSH-S-transferases (GSTs). The heterogeneous nature of CRC raises the questions of if the capacity of CRC cells to cope with increased ROS production during metastasis is context dependent and if it is influenced by genetic background. In the present study, we have used a large collection of tissue specimens from patients with metastatic CRC, a panel of patient-derived organoids (PDOs), and PDO-initiated metastasis models in mice to address these questions.

RESULTS

$BRAF^{V600E}$ CRC displays increased levels of GCLC and of reduced GSH

To start exploring a potential relationship between the reductive capacity of tumor cells and specific genetic alterations in CRC, we employed a series of PDOs (Table S1) and assessed the expression of a series of key redox-regulating genes in them. GSH synthetase (GS), GPX2, the catalytic and modifier subunits of glutamate-cysteine ligase (GCLC and GCLM), thioredoxin reductase (TXNRD1), and activated (phosphorylated) NRF2.

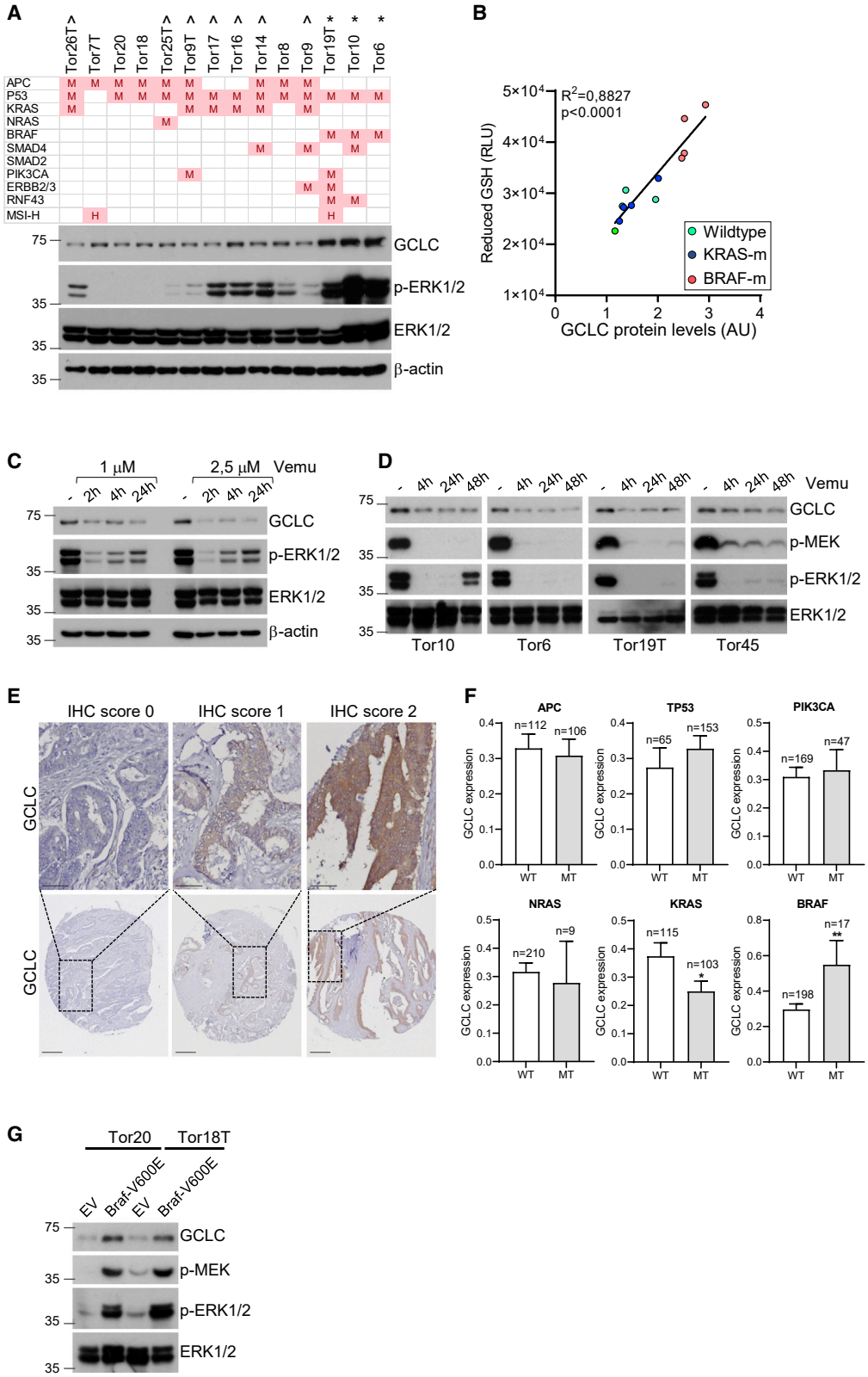

(legend on next page)

Comparison of the driver mutations in each of the PDOs with expression of these factors revealed that expression of GCLC protein, the catalytic subunit of the rate-limiting enzyme in GSH synthesis, correlated with the presence of $BRAF^{V600E}$ (Figures S1A and 1A). No other correlations were identified. The levels of reduced GSH showed a significant correlation with GCLC protein levels among PDOs (Figure 1B). In addition, PDOs with $BRAF^{V600E}$ expressed the highest levels of GCLC and contained the highest levels of reduced GSH when compared with wild-type or KRAS-mutant PDOs (Figures 1B, S1B, and S1C).

The V600E mutation in BRAF causes constitutive activation of its kinase activity and this can be inhibited with BRAF inhibitors like vemurafenib. Vemurafenib treatment of $BRAF^{V600E}$ PDOs caused a dose-dependent reduction of GCLC protein levels and inhibition of downstream MEK and ERK1/2 phosphorylation in 4 independent $BRAF^{V600E}$ PDOs (Figures 1C and 1D). To assess the clinical relevance of the association between GCLC expression and the presence of $BRAF^{V600E}$, we measured GCLC protein expression in a large cohort of metastatic CRC with driver gene mutation data and mismatch repair status (Table S2)[26,27] by immunohistochemistry using a tissue microarray (TMA). The specificity of the antibody was assessed by immunohistochemistry (IHC) analysis of GCLC expression on experimental GCLC-knockout tumors (see Figures S3A and S3B). GCLC expression in CRC was highly variable (Figure 1E). Driver gene mutation analysis revealed that only the presence of $BRAF^{V600E}$ was significantly positively correlated with high GCLC expression (Figure 1F). To establish the potential direct effect of $BRAF^{V600E}$ on GCLC expression, we transduced 2 wild-type PDO lines (Tor20 and Tor18T) with a lentiviral vector driving expression of GFP (control) or GFP and $BRAF^{V600E}$. Expression of $BRAF^{V600E}$ caused constitutive activation (phosphorylation) of its downstream targets MEK and ERK1/2 (Figure 1G) and increased expression of GCLC in both PDOs (Figure 1G).

GSH synthesis promotes organ-site-specific metastasis formation in $BRAF^{V600E}$ CRC

The presence of $BRAF^{V600E}$ in CRC is associated with an increased chance of distant metastasis formation. To investigate a potential role for GSH synthesis in $BRAF^{V600E}$-driven metastasis formation, we generated CRISPR-Ecas9-engineered GCLC (catalytic subunit) or GCLM (modifier subunit) knockout variants of PDOs carrying the V600E mutation in BRAF (Figures S2A and S2B). All GCLC- and GCLM-knockout PDOs showed a strong and significant decrease in endogenous reduced GSH levels (Figure 2A). All PDO variants were subsequently transduced with a lentiviral vector expressing firefly luciferase, allowing non-invasive bioluminescence imaging (BLI) of tumor load and dissemination. During routine passaging, GCLC- and GCLM-knockout clones retained similar proliferative capacity and viability when compared with control organoids expressing Ecas alone (Figure 2B). In addition, GCLC or GCLM knockout did not impair their capacity to initiate subcutaneous tumors (Figures S2C and S2D).

To study the impact of impaired GSH synthesis on spontaneous metastasis, we generated a model using orthotopic transplantation of PDOs into the submucosa of the caecum wall of immune-deficient mice (Figure 2C[28]). This model was chosen because BRAF mutant tumors are significantly more prevalent in the proximal (right-sided) part of the large intestine, which includes the caecum.[29] Pilot experiments with the parental PDOs had indicated that primary tumors form with high efficiency and cause spontaneous formation of distant metastases in the liver, the lung, and the peritoneum (Figure 2C). Transplantation of control, GCLC-knockout (KO), or GCLM-KO PDOs resulted in 85%–100% tumor take without significant differences between experimental groups (Figures S2E and S2F). Primary caecum tumors were first detected between 3 and 4 weeks after transplantation (Figure S2E). There were no significant differences in primary caecum tumor growth between control Ecas or GCLC- or GCLM-KO groups using *ex vivo* organ-specific BLI measurements (Figures 2D and 2E).

Metastatic lesions were first detected by BLI approximately 6–9 weeks following organoid transplantation (Figure S2E). After 12–16 weeks, mice were sacrificed, and all relevant organs were harvested and analyzed for tumor growth and metastasis formation using *ex vivo* organ-specific BLI and IHC with anti-human pan-cytokeratin (pan-CK) or anti-human nucleoli (hNuc). Mice transplanted with control organoids developed distant

Figure 1. $BRAF^{V600E}$ CRC displays increased levels of GCLC and of reduced glutathione

(A) Immunoblot analysis of GCLC, phospho-ERK1/2 (p-ERK1/2), total ERK1/2, and β-actin expression levels in Laemmli lysates derived from a selection of CRC patient-derived organoid (PDO) lines. ^ indicates KRAS or NRAS-mutant PDO lines; * indicates $BRAF^{V600E}$-mutant PDO lines. The unlabeled PDOs are double wild type (WT) for RAS/BRAF. Data are representative of three independent experiments.

(B) Correlation between intracellular glutathione levels and GCLC protein expression in PDOs. Green dots mark WT PDOs, blue dots mark KRAS-mutant, and red dots mark $BRAF^{V600E}$-mutant PDOs. RLU, relative luminescence unit; AU, arbitrary unit. All data are the average of at least two biological replicates, and each dot represents the mean of three technical replicates of each experiment. R squared and p values were determined by correlation analysis test.

(C) Immunoblot analysis of GCLC, phospho-ERK1/2, total ERK1/2, and β-actin in Tor10 PDOs following treatment with the BRAF inhibitor vemurafenib at the indicated concentrations and time points. Data are representative of at least two independent experiments.

(D) Immunoblot analysis of GCLC, phospho-MEK (p-MEK), phospho-ERK1/2, and total ERK1/2 levels in Tor10, Tor6, Tor19T, and Tor45 $BRAF^{V600E}$-mutant-bearing PDOs following treatment with vemurafenib (2.5 or 5 μM) at the indicated time points. Data are representative of at least two independent experiments.

(E) Immunohistochemistry analysis of GCLC expression in tissue microarrays (TMAs) of metastatic CRC (CAIRO3 cohort) using a validated antibody (see Figure S3). Examples show tumors with weak (0), intermediate (1), and strong (2) GCLC expression. Scale bars, 200 and 50 μm.

(F) As in (E), graphs showing the average GCLC staining intensity in subgroups of tumors with WT or mutations (MTs) in the indicated specific genetic driver genes. The bar graphs show means ± SEM. Significant differences between groups were determined by unpaired Student's t tests (*$p < 0.05$, **$p < 0.005$). The numbers of tumors analyzed for each group are indicated in the bars.

(G) Immunoblot analysis of GCLC, p-MEK, p-ERK1/2, and total ERK1/2 protein expression in Laemmli lysates derived from WT Tor20 and Tor18T PDOs transduced with either lentiviral FG12-GFP empty vector (EV) or with FG12-GFP-BRAFV600E vector expressing mutant $BRAF^{V600E}$. Data are representative of two independent experiments. See also Figure S1.

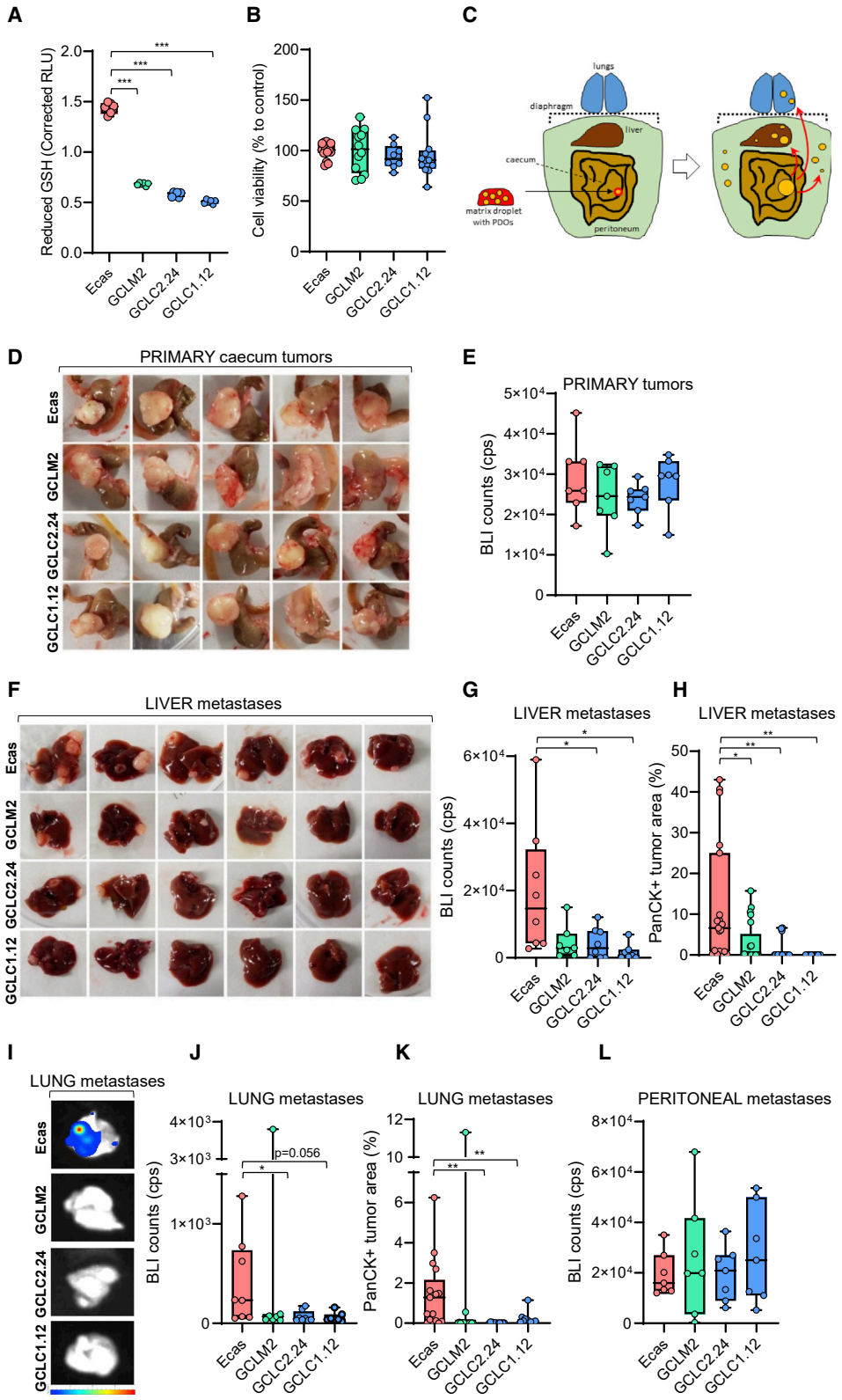

(legend on next page)

metastases in the liver, lungs, and peritoneal cavity. The high variability of metastasis formation among mice transplanted with control (ECAS) PDOs (Figures 2F–2K) is presumably due to the stochastic and continuous nature of metastasis formation in this model. By contrast, in more commonly applied models, all metastases are seeded at once by a single injection of a large number of tumor cells into the circulation. There was no detectable metastasis formation in the brain or bones. Organ-specific BLI measurements and pan-CK IHC revealed a strong reduction of metastases in the liver and the lungs of mice transplanted with GCLC-KO PDOs when compared with mice transplanted with control PDOs (Figures 2F–2K and S2F-S2L). Mice transplanted with GCLM-KO organoids also displayed reduced metastasis formation in the liver and the lungs, albeit to a lesser extent (Figures 2F–2K). Anti-pan-CK and anti-hNuc IHC revealed a strong decrease in the number and the size of established metastatic lesions. By contrast, the formation of peritoneal metastases was not significantly affected by KO of GCLC or GCLM (Figures 2L and S2F).

To distinguish between an early effect of GCLC and GCLM KO on initial seeding of liver and lung metastases versus a late effect on subsequent outgrowth, we performed anti-hNuc IHC to detect all metastases of all sizes in both organs in mice transplanted with control (Ecas), GCLC-KO, and GCLM-KO PDOs. This analysis revealed that the vast majority of mice transplanted with GCLC-KO PDOs had no detectable liver metastases (of any size), indicating a major reduction in initial seeding capacity (Figures S2G–S2I). Lungs in mice transplanted with GCLC-KO PDOs did contain detectable metastases, but their size was considerably smaller than that of control (Ecas) (Figures S2J–S2L). The few liver and lung lesions that were established from GCLC-KO PDOs were significantly smaller than control (Ecas) metastases and had fewer Ki67-positive (proliferating) cells, also indicating a reduced outgrowth capacity (Figures 3A–3D). GCLM-KO liver and lung metastases showed an intermediate reduction of Ki67-positive cells (Figures 3A–3D). GCLC or GCLM KO had no significant impact on tumor cell proliferation in primary caecum tumors or peritoneal metastases (Figures S3A and S3B).

Next, we used phosphorylated histone 2AX (γ-H2AX) as a measure of DNA damage (double-strand breaks). GCLC-KO liver metastases showed a significant increase in the number of γH2AX-positive cells when compared with Ecas control metastases, but this was not observed in GCLM-KO metastases (Figures 3E and 2F). An increase in the number of γH2AX-positive cells could be due to hypoxia-induced oxidative stress or to DNA breaks that occur during apoptosis. However, neither the hypoxia marker CAIX nor the apoptosis marker cleaved-caspase-3 (Cl-CASP3) were significantly different between Ecas control and GCLC-KO liver metastases (Figures S3C–S3F). In addition, neither CAIX staining nor the presence of necrotic tumor areas were significantly different between liver metastases and the corresponding peritoneal metastases (Figures S3G–S3I).

To obtain further evidence for a potentially selective requirement for the GSH pathway in liver and lung, but not peritoneal, metastasis formation, we made use of two additional spontaneous PDO-initiated CRC metastasis models that give rise to liver and peritoneal metastases (model TOR98) or lung and peritoneal metastases (model TOR1), respectively. RNA sequencing data of PDOs, subcutaneous tumors, primary caecum tumors, and corresponding metastatic lesions from all available sites were used to perform differential gene expression and pathway enrichment analyses. Using the Kyoto Encyclopedia of Genes and Genomes (KEGG; consisting of 551 biological pathways), we found that 62 and 51 pathways were significantly upregulated in liver or lung metastases when compared with primary tumors, respectively (Table S3). Of these, 15 pathways were enriched in both liver and lung metastases, including the "glutathione metabolism" pathway (hsa00480). Indeed, liver and lung metastases had significantly higher GSH metabolism pathway scores than PDOs, subcutaneous tumors, primary tumors, or peritoneal metastases (Figures S4A–S4D). Moreover, GCLC was expressed to higher levels in lung and liver metastases than in the corresponding primary tumors (Figures S4A–S4D).

Figure 2. GSH synthesis promotes organ-site-specific metastasis formation in BRAF^{V600E} CRC

(A) Luminescence measurements of intracellular reduced glutathione levels during exponential growth of Tor10-derived Ecas control PDOs, 2 independent GCLC-knockout PDOs (GCLC1.12 and GCLC2.24), and GCLM-knockout clone 2 (GCLM2). Statistical significance of the differences between groups was analyzed by unpaired Student's t tests (***$p < 0.0001$).

(B) ATP levels as a proxy for cell viability (percentage of control) during exponential growth of PDOs from each of the indicated genetic variants.

Data in (A) and (B) are representative of three independent experiments, and each dot represents the mean of three technical replicates of each experiment.

(C) Schematic representation of spontaneous metastasis model using orthotopic transplantation of PDOs into the submucosa of the caecum wall of immune-deficient mice.

(D) Control (Ecas), GCLM-KO (2), and 2 different GCLC-KO (1.12 and 2.24) PDOs were seeded in collagen droplets and subsequently implanted in the caecum wall of immune-deficient mice ($n \geq 7$ mice per group). Representative photographs showing caecum primary tumors from each group.

(E) The box and whisker plots (minimum [min] to maximum [max]; all data points) show *ex vivo* bioluminescence imaging (BLI) analysis of primary caecum tumors growing at the implantation site as in (D) ($n = 7$ mice per group).

(F) Representative photographs showing examples of liver metastases in each experimental group.

(G) Quantification of spontaneous liver metastasis formation in the same experiment as in (D) by *ex vivo* BLI of isolated livers. Each dot represents BLI counts of each individual liver in each experimental group (for Ecas, $n = 8$ mice; for GCLM2, $n = 7$ mice; for GCLC2.24, $n = 8$ mice; and for GCLC1.12, $n = 7$ mice).

(H) Quantification of spontaneous liver metastasis formation as in (G) by immunohistochemistry (IHC) analysis of the human tumor marker Pancytokeratin (PanCK). *$p < 0.05$, **$p < 0.005$, unpaired Student's t tests.

(I) Representative BLI measurement of lung metastasis in each experimental group.

(J and K) Quantification of spontaneous lung metastasis using *ex-vivo* BLI measurement (J) and panCK IHC (K) as in (G) and (H). *$p < 0.05$, **$p < 0.005$, unpaired Student's t tests. (For Ecas, $n = 8$ mice; for GCLM2, $n = 7$ mice; for GCLC2.24, $n = 8$ mice; and for GCLC1.12, $n = 7$ mice).

(L) Quantification of peritoneal metastasis formation by *ex-vivo* BLI in the same experiment as in (D). ($n = 7$ mice per group). All IHC sections were quantified using QuPath software. See also Figure S2.

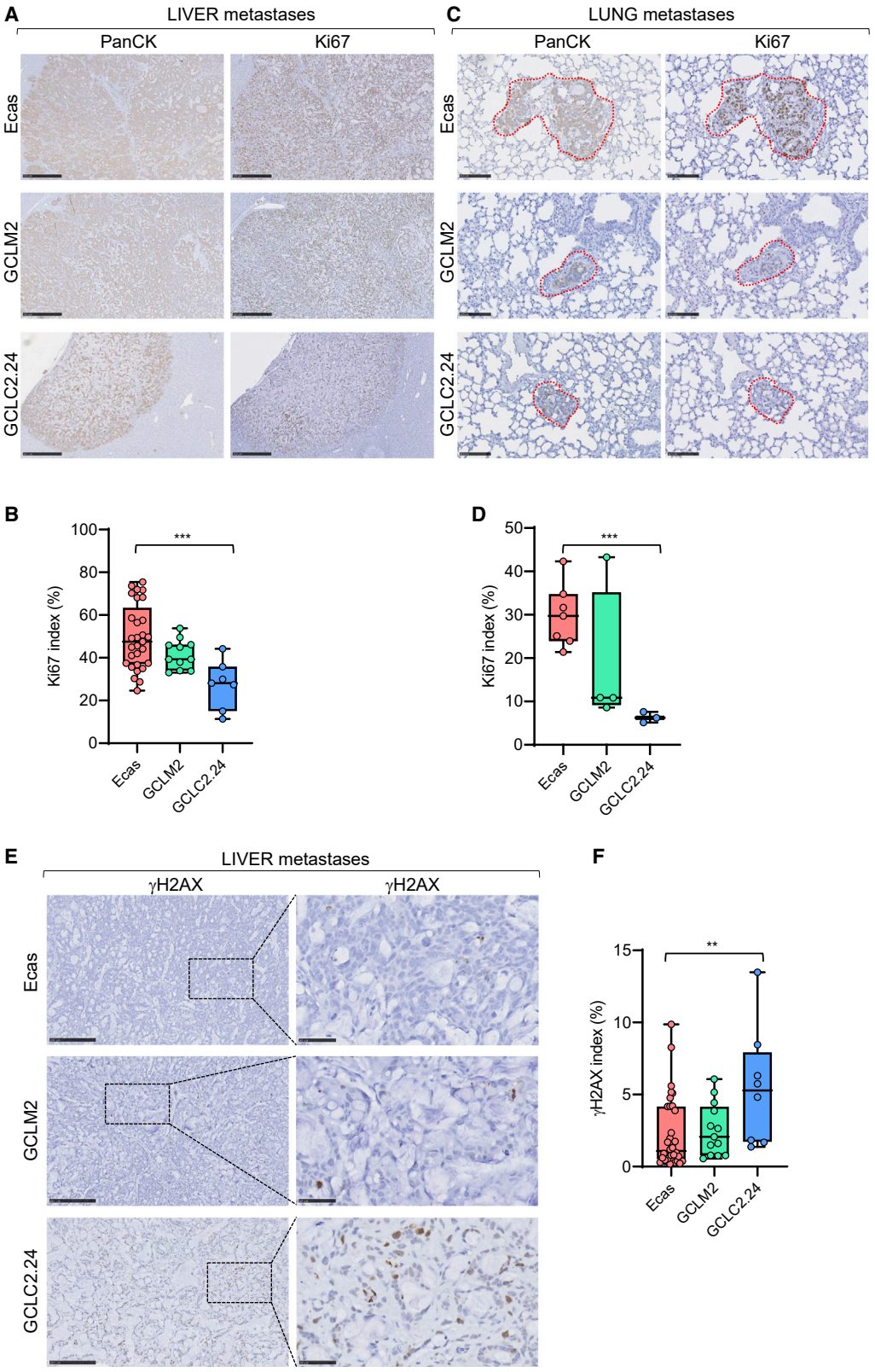

(legend on next page)

N-acetylcysteine boosts GSH synthesis and stimulates organ-site-specific metastasis in BRAF^{V600E} CRC

The above results demonstrate how impaired GSH synthesis reduces spontaneous metastasis formation to the liver and the lungs. We next tested whether boosting GSH synthesis would have the opposite effect. To this end, we used N-acetylcysteine (NAC), a precursor for cellular GSH. One week after caecum transplantation of TOR10 PDOs, mice were treated with NAC or vehicle. Primary tumor formation in the caecum and metastasis formation were then assessed 12–16 weeks after transplantation. NAC treatment had no significant effect on the initiation or outgrowth of primary caecum tumors (Figures 4A, S5A, and S5B). In addition, pre-treatment of mice with NAC before tumor transplantation in the caecum did not affect primary tumor growth (Figure S5C). However, NAC-treated mice displayed increased distant metastasis formation in the liver and the lungs when compared with control-treated mice (Figures 4B–4F and S5D). Strikingly, NAC-treated mice displayed metastasis formation in the brain, which had never been observed before in this model (Figure 4E). By contrast, metastasis formation in the peritoneum was not significantly altered by NAC treatment (Figure 4G). IHC for Ki67 revealed that liver and lung metastases from NAC-treated mice contained significantly more Ki67-positive proliferating cells than metastases from control-treated mice (Figures 4H and 4I). NAC treatment also caused a significant increase in the number of apoptotic cells in liver metastases, measured by anti-Cl-CASP3 IHC (Figures S5E and S5F). The apoptotic cells were mainly localized around necrotic tissue areas, typically present in the larger (faster growing) liver metastases in NAC-treated mice. This effect was not observed in lung metastases, presumably because of their smaller size (Figures S5G and S5H).

Cysteine, derived from NAC, is a precursor for GSH synthesis. To assess the effect of NAC on GSH synthesis, we measured intracellular GSH levels in control- and NAC-treated mice. IHC for GSH revealed an increase in GSH levels in liver and lung metastasis derived from NAC-treated mice when compared with control-treated metastases (Figures 4J-4L). The specificity of GSH staining was confirmed in GCLC-KO-derived primary tumors and liver metastases that showed decreased GSH levels when compared with Ecas control tumors (Figure S6A). To confirm the direct contribution of NAC on boosting GSH synthesis, we measured intracellular GSH levels in Ecas control, GCLC-KO, and GCLM-KO PDOs following treatment with increasing concentrations of NAC. Basal intracellular levels of GSH were significantly lower in GCLC-KO and GCLM-KO PDOs compared with control (Ecas) PDOs. In addition, NAC treatment caused a strong and significant increase in GSH production in control (Ecas) PDOs but not in GCLC-KO or GCLM-KO PDOs (Figure S6B). Next, we assessed the effect of NAC on metastasis formation in mice transplanted with either control (Ecas) or GCLC-KO (GCLC1.12) PDOs. Mice transplanted with control (Ecas) or GCLC-KO PDOs were treated with either saline or NAC solution 1 week after tumor transplantation for 16 weeks. NAC treatment caused increased formation of liver and lung metastases in mice transplanted with control (Ecas) PDOs but had no effect on metastasis formation in mice transplanted with GCLC-KO PDOs (Figures 4M–4O).

In addition to its effects on GSH synthesis, NAC can also cause activation of the MAPK pathway.[30] To test whether this may have contributed to increased metastasis formation, we assessed the effect of NAC on intracellular p-ERK levels in liver and lung metastases. The levels of p-ERK were not significantly different between liver metastases from control- and NAC-treated mice (Figures S6C and S6D). However, we did observe a near-significant increase in p-ERK levels in lung metastases from NAC-treated mice compared with control mice (Figures S6E and S6G).

BRAF^{V600E} CRC PDOs display increased resistance to oxidative stress

The above data implicate GSH synthesis in metastasis formation in the liver and lungs by BRAF^{V600E}-expressing tumor cells, but they do not formally prove that BRAF^{V600E} protects tumor cells against oxidative stress. To address this directly, we experimentally induced oxidative stress in PDOs by combined pharmacological targeting of the GSH pathway and the thioredoxin (TXN) pathway[31–33] using buthionine sulfoximine (BSO) and auranofin, respectively. Dose response assays revealed a highly variable sensitivity between individual PDO lines to oxidative stress (Figures 5A and 5B). BSO treatment strongly reduced the IC50 for auranofin in all PDOs tested (Figures 5A–5C). Strikingly, of all 18 PDOs tested, the 4 BRAF^{V600E} organoids were significantly more resistant to oxidative-stress-inducing drugs than BRAF wild-type organoids, as the IC50 for auranofin showed the lowest decrease in BRAF^{V600E} organoids after BSO addition (Figures 5D and 5E).

Figure 3. Impaired GSH synthesis decreases proliferation and increases DNA damage in liver and lung metastases

(A) IHC analysis of the tumor marker Pancytokeratin (PanCK) and the proliferation marker Ki67 in tissue sections of liver metastases formed by control Ecas, GCLM-KO and GCLC-KO tumors. Anti-human pan-cytokeratin (panCK) was used to identify macro- and micro-metastases within the tissue sections. Scale bars, 500 μm.

(B) Box and whisker plots (all data) of Ki67-positive tumor cells in liver metastases in the indicated groups. Significant differences between groups were determined by unpaired Student's t tests (***$p < 0.001$). Each dot represents individual tumor lesion analyzed per liver section in each experimental group. (For Ecas, n = 29 lesions; for GCLM2, n = 11 lesions; and for GCLC2.24, n = 7 lesions).

(C) IHC analysis of Ki67 in tissue sections of lung metastases in the indicated groups. Identification of metastases and quantification of staining was performed as in (A). Scale bars, 100 μm.

(D) Box and whisker plots (all data) of Ki67-positive tumor cells in lung metastases in the indicated groups. ***$p < 0.001$, unpaired Student's t tests. Each dot represents average Ki67 index per lung section per mouse in each experimental group. (For Ecas, n = 7 mice; for GCLM2, n = 4 mice; and for GCLC2.24, n = 3 mice).

(E) IHC analysis of the DNA damage marker γ−H2AX in tissue sections of liver metastases in the indicated groups. Scale bars, 250 μm and 50 μm respectively.

(F) Box and whisker plots (all data) of γ−H2AX-positive tumor cells in liver metastases in the indicated groups. QuPath was used to quantify the extent of staining. **$p = 0.0057$, unpaired Student's t tests. Each dot represents individual tumor lesion analyzed per liver section in each experimental group. (For Ecas, n = 34 lesions; for GCLM2, n = 13 lesions; and for GCLC2.24, n = 8 lesions). See also Figure S3.

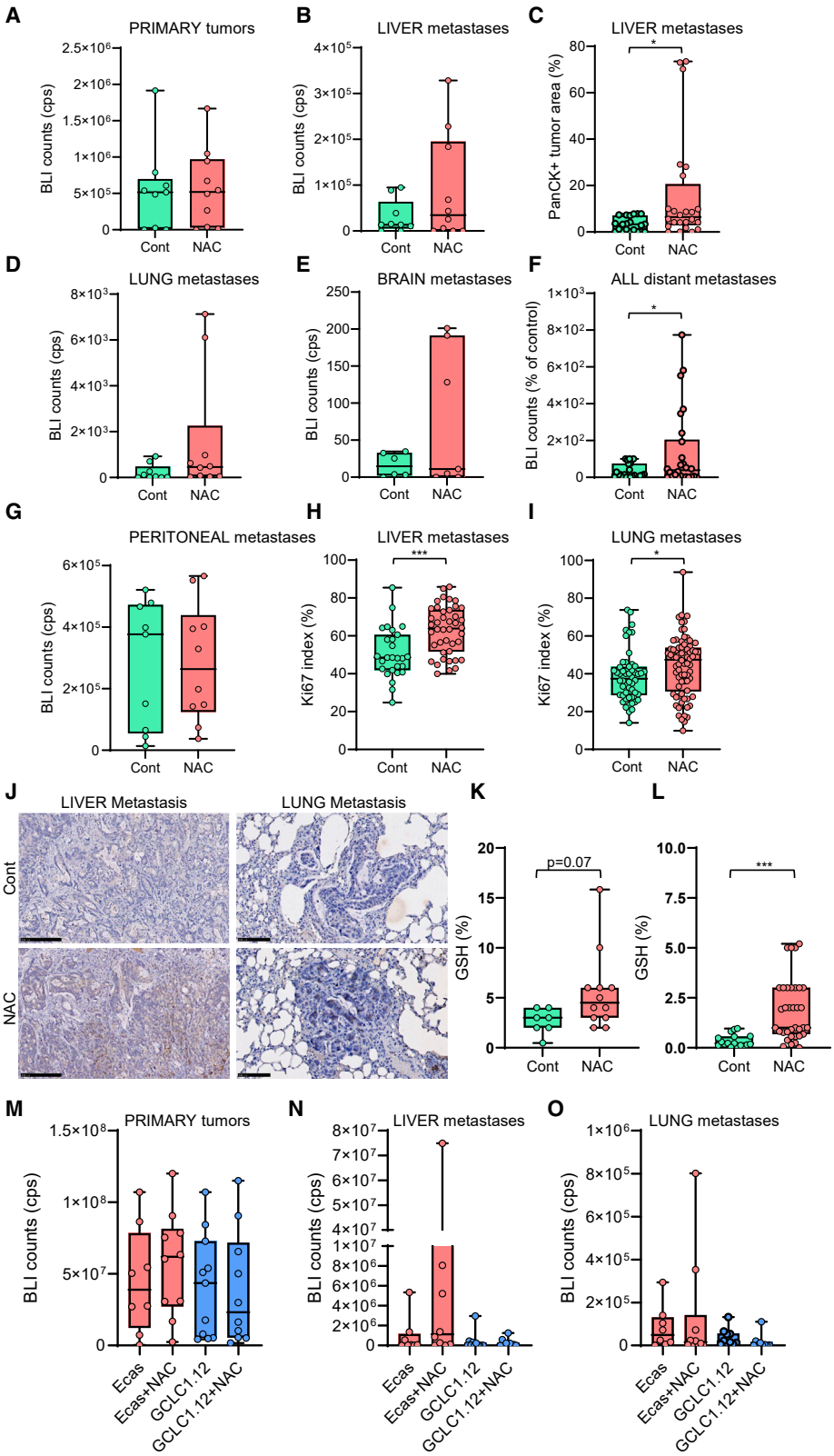

(legend on next page)

Sensitivity to oxidative stress was significantly correlated with GCLC protein expression (Figure 5F) and with the levels of reduced GSH in PDOs before and after treatment (Figures 5G and 5H). Treatment with BSO alone or in combination with auranofin efficiently depleted intracellular GSH (Figure 5I), and this could partially be reverted by the supplementation of either reduced GSH or NAC (Figure 5J). However, only the combination treatment caused an increase in H_2O_2 levels prior to the onset of cell death (Figure 5K). The latter finding is in line with the notion that both the GSH and TRX pathways need to be inhibited simultaneously in order to induce oxidative stress.

While drugs can be used to artificially induce oxidative stress in tumor cells, during metastasis it is caused, at least in part, by the loss of cell-cell adhesion. Therefore, we induced oxidative stress in PDOs by disrupting cell-cell contacts in the presence or absence of BSO and analyzed the capacity of $BRAF^{V600E}$ and wild-type PDOs to regenerate organoids. BSO treatment alone did not interfere with proliferation and survival of actively growing organoids, regardless of BRAF status (Figure S7A). However, following disruption of cell-cell contacts, BSO treatment significantly reduced the long-term regenerative capacity of BRAF wild-type PDOs but not that of $BRAF^{V600E}$ PDOs (Figures S7B and S7C).

Sensitization of $BRAF^{V600E}$ PDOs to oxidative stress by blocking GSH synthesis and inhibition of BRAF kinase activity

Since the relative resistance of $BRAF^{V600E}$ PDOs to oxidative stress correlated with high expression of GCLC and with high intracellular GSH levels (Figure 5), we reasoned that the BSO concentrations used may have been too low to completely inhibit GCLC in $BRAF^{V600E}$ PDOs. Indeed, higher concentrations of BSO caused a dose-dependent sensitization of $BRAF^{V600E}$ PDOs to auranofin (Figure 6A). Even at these high concentrations, BSO had no effect on cell viability during routine organoid culturing (Figure 6B).

To further study the role of GSH synthesis in the protection against oxidative stress in $BRAF^{V600E}$ PDOs, we made use of the GCLC- and GCLM-KO PDOs. Both GCLC and GCLM KO sensitized $BRAF^{V600E}$ PDOs to auranofin treatment (Figures 6C–6E). Moreover, overexpression of FLAG- or GFP-tagged GCLC in the most sensitive (BRAF wild type) PDO (TOR26T) caused a significant protection against oxidative stress (Figures 6F and 6G). Finally, exogenous expression of $BRAF^{V600E}$ in Tor20 and Tor18T (BRAF wild type) PDOs caused a significant protection against auranofin-BSO combination treatment (Figures 6H–6M).

In Figure 1, we show that inhibition of BRAF activity with vemurafenib reduced GCLC expression in mutant BRAF PDOs. Therefore, BRAF inhibition may sensitize $BRAF^{V600E}$ organoids to oxidative stress. To test this, oxidative stress was induced in three $BRAF^{V600E}$ PDOs by using BSO and increasing concentrations of auranofin. All three $BRAF^{V600E}$ PDOs showed increased sensitivity to BSO-auranofin combination treatment after treatment with vemurafenib (Figures 7A–7D).

Finally, we tested whether the observed connection between $BRAF^{V600E}$ in CRC and high reductive capacity could offer an

Figure 4. N-acetylcysteine-dependent increase of intracellular GSH stimulates organ-site-specific metastasis formation in $BRAF^{V600E}$ CRC

(A) Luciferase-expressing Tor10 PDOs were seeded into collagen droplets and were subsequently implanted in the caecum wall of immune-deficient mice ($n \geq 9$ mice per group) as in Figure 2. N-acetylcysteine (NAC) was administered intraperitoneally at 1 g/kg 3 times a week, starting 1 week after caecum implantation. Box and whisker plots show a quantification of *ex-vivo* BLI measurements of isolated primary caecum tumors. Each dot represents BLI counts of each individual organ per mouse in each experimental group. (For control, n = 9 mice; and for NAC, n = 10 mice).

(B) Quantification of spontaneous liver metastasis formation in the same experiment by *ex-vivo* BLI measurement of isolated livers (all mice). (For control, n = 9 mice; and for NAC, n = 10 mice).

(C) Quantification of spontaneous liver metastasis formation in the same experiment by immunohistochemistry (IHC) using anti-human pan-cytokeratin. IHC sections (all mice) were quantified using QuPath software. Statistical significant differences between groups were determined by unpaired Student's t test (*$p < 0.05$). Each dot represents individual tumor lesion analyzed per liver section in each experimental group (for control, n = 21 lesions, and for NAC, n = 24 lesions).

(D) As in (B) for lung metastases (for control, n = 9 mice, and for NAC, n = 10 mice).

(E) As in (B) for brain metastases (for control, n = 6 mice, and for NAC, n = 7 mice).

(F) Aggregate analysis of the relative increase in metastasis formation in liver, lungs, and brain based on *ex vivo* BLI data. The highest values in the control group of each organ were set to 100%. Each dot represents individual organ analyzed per mouse in each experimental group (for control, n = 24, and for NAC, n = 26). *$p < 0.05$, unpaired Student's t test.

(G) As in (B) for peritoneal metastasis (for control, n = 9 mice, and for NAC, n = 10 mice).

(H) Box and whisker plots (all mice) of Ki67-positive tumor cells using IHC analysis in tissue sections of liver metastases. QuPath was used to quantify the extent of staining. ***$p < 0.001$, unpaired Student's t test. Each dot represents individual tumor lesion analyzed per liver section in each experimental group (for control, n = 27 lesions, and for NAC, n = 42 lesions).

(I) As in (H) for lung metastasis. *$p < 0.05$, unpaired Student's t test. Each dot represents individual tumor lesion analyzed per lung section in each experimental group (for control, n = 52 lesions, and for NAC, n = 74 lesions).

(J) Representative pictures of IHC staining of GSH in liver and lung metastasis derived from control or NAC-treated mice. Scale bars, 250 (liver) and 100 μm (lung).

(K) Box and whisker plots of the quantification of GSH expression in liver metastases expressed as the percentage of positive area. Each dot represents individual tumor lesion analyzed per liver section in each experimental group (for control, n = 7 lesions, and for NAC, n = 12 lesions).

(L) As in (K) for lung metastases. ***$p < 0.001$, unpaired Student's t test. Each dot represents individual tumor lesion analyzed per lung section in each experimental group (for control, n = 17 lesions, and for NAC, n = 35 lesions).

(M) Control (Ecas) and GCLC-KO (GCLC1.12) PDOs were seeded in collagen droplets and subsequently implanted in the caecum wall of immune-deficient mice ($n \geq 8$ mice per group). The box and whisker plots (min to max; all data points) show *ex vivo* BLI analysis of primary caecum tumors growing at the implantation site. Each dot represents BLI counts of each individual organ per mouse in each experimental group (for Ecas, n = 8 mice; for Ecas + NAC, n = 10 mice; for GCLC1.12, n = 11 mice; and for GCLC1.12 + NAC, n = 10 mice).

(N) As in (M) for liver metastasis.

(O) As in (M) for lung metastasis (see also Figures S5 and S6).

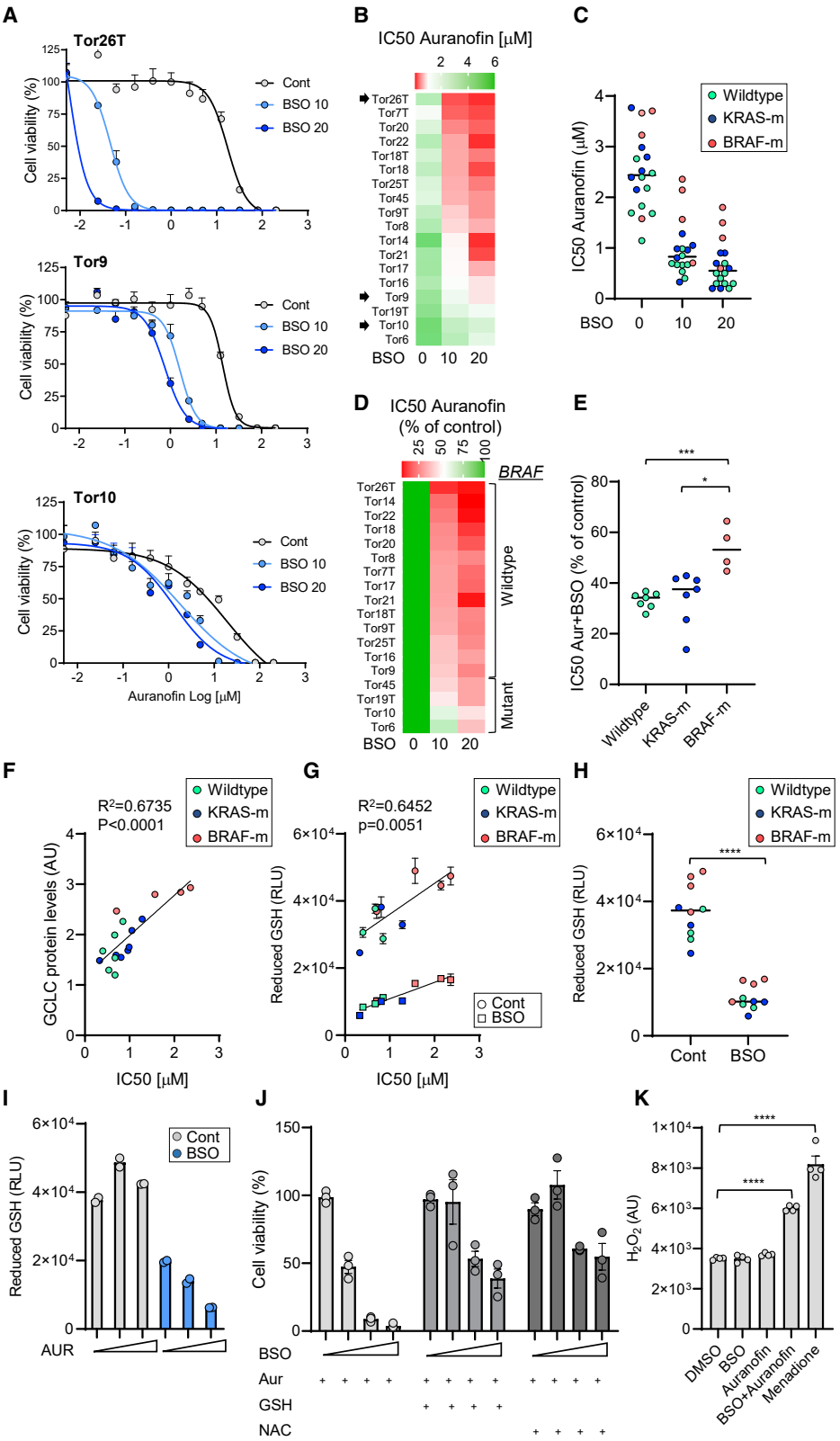

(legend on next page)

alternative strategy for sensitizing these tumors to BRAF inhibition. To this end, we analyzed how treatment of 3 $BRAF^{V600E}$ PDOS with BSO and auranofin would affect their response to increasing concentrations of vemurafenib. Vemurafenib treatment alone, or in combination with auranofin, only marginally reduced the viability of $BRAF^{V600E}$ PDOs. However, further addition of BSO caused a dramatic sensitization of all three $BRAF^{V600E}$ PDOs to vemurafenib (Figures 7E–7G and S7D). These results demonstrate that lowering the reductive capacity of $BRAF^{V600E}$ PDOs by simultaneous targeting of the GSH and the TXN systems is an efficient strategy to sensitize them to vemurafenib treatment.

DISCUSSION

$BRAF^{V600E}$ is associated with distant metastasis formation.[34–37] In this study, we identified the GSH-synthesizing enzyme GCLC as an essential mediator of distant metastasis formation to the liver and lungs in a PDO model of $BRAF^{V600E}$ metastatic CRC. Our finding that $BRAF^{V600E}$ counteracts oxidative stress by stimulating GCLC expression and GSH synthesis may (partially) explain the metastasis-prone behavior of $BRAF^{V600E}$ tumors. Although this study was focused on GCLC, other enzymes involved in the synthesis or utilization of GSH (e.g., GS, GXPs, GSH transferases) may also have an impact on distant metastasis. In contrast to V600E, non-V600 mutations in BRAF are associated with a better prognosis in CRC.[8] Future studies are therefore needed to assess the impact of such mutations on GCLC expression and GSH synthesis in relation to metastatic capacity. Surprisingly, GCLC expression was significantly lower in KRAS mutant CRC. Differences in signaling between $BRAF^{V600E}$ and mutant KRAS[9,38] may translate into distinct effects on GCLC expression.

CRC cells require GSH synthesis, which is stimulated by $BRAF^{V600E}$ (this study), in order to form liver metastases.[18,21] As a result, $BRAF^{V600E}$-expressing cells are likely to remain fitter in the face of pro-oxidant challenges at distant organ sites. Hypoxia is a potential source of oxidative stress in the liver, as it triggers ROS generation.[39,40] However, hypoxia also induces GCLC expression and GSH synthesis.[41] Nevertheless, even successfully formed liver metastases sustain higher levels of oxidative damage when compared with their paired primary tumors.[42] Since expression of the hypoxia marker CAIX was similar between primary tumors and liver metastases, factors other than hypoxia are likely to be more important in causing oxidative damage associated with liver metastasis formation, for instance the loss of cell-cell and cell-matrix contacts.[15–17]

Disseminated tumor cells that arrive in the lungs also face a highly pro-oxidant microenvironment.[43,44] In breast cancer models, lung metastasis is supported by upregulation of PPARγ coactivator 1α (PGC-1α),[45] which stimulates expression of antioxidant genes,[46] or by the antioxidant peroxiredoxin-2.[47] Our study shows that CRC cells rely on GCLC and GSH synthesis for successful lung metastasis. Indeed, systemic administration of the GSH precursor and antioxidant NAC promotes the formation of primary lung tumors[23,48] and liver and lung metastases in CRC (this study). In addition, we found that NAC stimulated the formation of brain metastases, possibly resulting from the high tumor load in these mice. Alternatively, GSH synthesis may specifically stimulate metastasis formation in the brain as it does in

Figure 5. $BRAF^{V600E}$ PDOs display increased resistance to oxidative stress

(A) Dose-response curves of PDOs to increasing concentrations of auranofin alone or in combination with BSO at the indicated concentrations (in μM). Data are presented as means ± SEM and are representative of at least three independent experiments, and each dot represents the mean of three technical replicates of each experiment.

(B) Heatmap plot showing IC50 values based on dose-response curves of all tested PDOs to auranofin treatment alone or in combination with BSO (10 and 20 μM). IC50 values are average of at least three independent experiments. Arrows indicate the examples shown in (A).

(C) Graph showing IC50 values to auranofin alone or in combination with BSO (10 and 20 μM) of all tested PDOs as those presented in (B), sub-grouped according to their KRAS and BRAF mutational status. Green dots mark WT PDOs, blue dots mark KRAS-mutant (KRAS-m), and red dots mark $BRAF^{V600E}$-mutant (BRAF-m) PDOs.

(D) Heatmap plot showing the IC50 values (set as percentage of control) for single-drug treatment with auranofin (set to 100%) or in combination with BSO (10 and 20 μM) of all tested PDOs as those presented in (B).

(E) Dot plot showing the IC50 values for auranofin after addition of BSO (10 μM) (set as percentage of control) as presented in (D) of all tested PDOs sub-grouped according to their KRAS and BRAF mutational status. Significant differences between groups were determined by unpaired Student's t tests (*$p < 0.05$, ***$p < 0.0005$).

(F) Correlation of GCLC protein expression (AU) quantified by density scans of western blot signals using ImageJ software, and sensitivity to auranofin/BSO combination treatment, expressed as the IC50 value for each PDO. R squared and p values were determined by correlation analysis test.

(G) Correlation between intracellular glutathione levels and auranofin/BSO IC50 in a selection of PDO lines treated with vehicle (circle dots) or with BSO (square dots) for 24 h. The bar graphs show means ± SEM. Data are average of at least two biological replicates, and each dot represents the mean of two technical replicates of each experiment. R squared and p values were determined by correlation analysis test.

(H) Intracellular levels of reduced glutathione in PDOs that were treated with control or with BSO for 24 h, as determined in (G). ****$p < 0.0001$, unpaired Student's t test.

(I) Quantification of intracellular glutathione levels in Tor26T PDOs treated for 24 h with control or Auranofin (1.5 or 3 μM) alone or in combination with BSO (10 μM). The bar graphs show means ± SEM. Data are average of at least two biological replicates, and each dot represents the mean of two technical replicates of each experiment.

(J) ATP levels as a proxy for the amount of live cells (percentage of control) following a 72 h treatment of 3-day-old Tor26T PDOs with auranofin (1 μM) alone or in combination with increasing concentrations of BSO (5, 10, and 20 μM) and in the presence or absence of NAC or reduced GSH. The bar graphs show means ± SEM. Data are average of at least two biological replicates, and each dot represents the mean of three technical replicates of each experiment.

(K) Quantification of H_2O_2 levels in control-, auranofin-, and BSO-treated PDOs (Tor26T). Menadione (25 μM), a ROS-inducing agent, was used as a positive control. AU, arbitrary units. All data are presented as means ± SEM and are representative of three biological replicates; each dot represents the mean of three technical replicates of each experiment. ****$p < 0.0001$, unpaired Student's t tests.

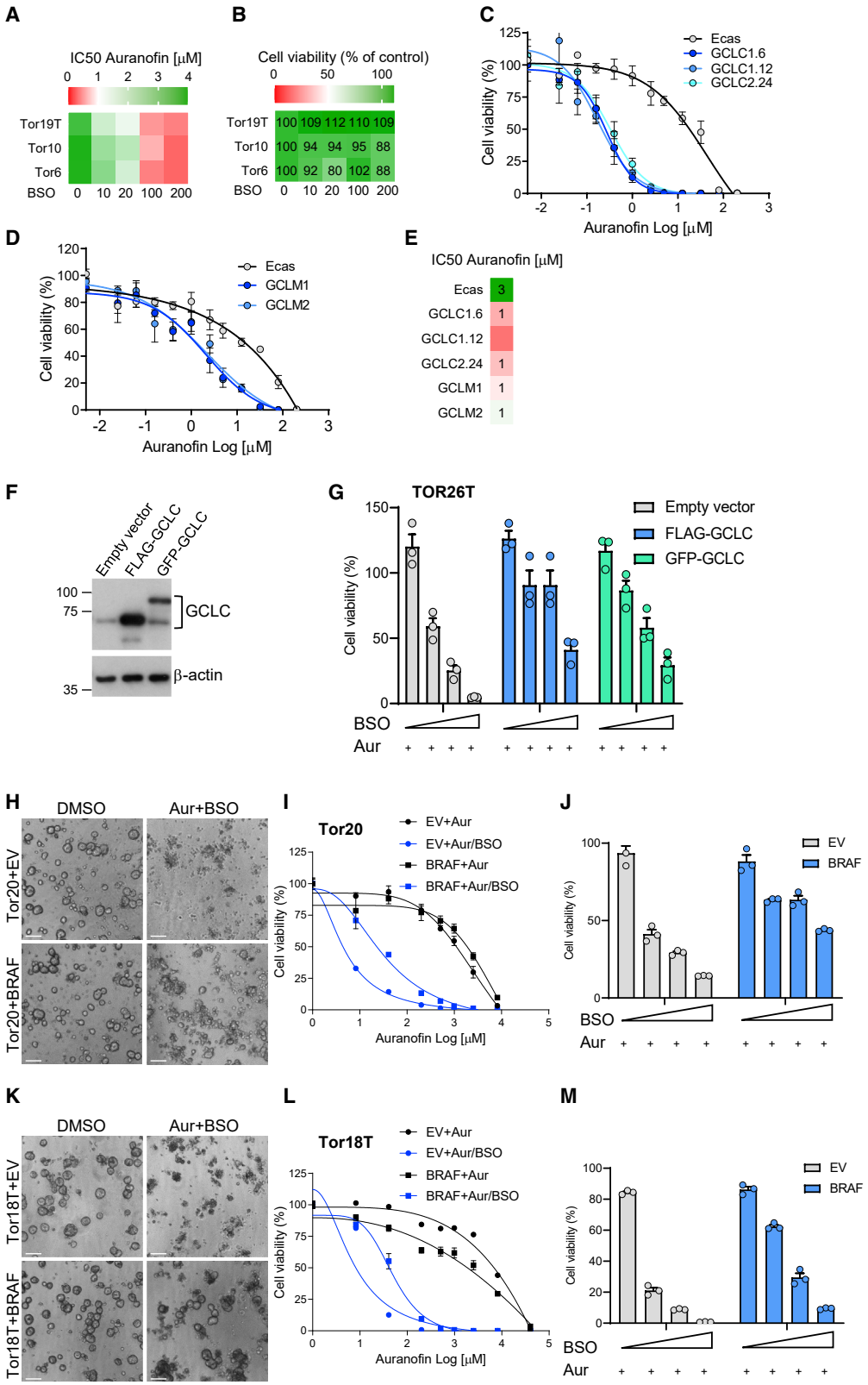

(legend on next page)

the liver and lungs. At present, it is difficult to distinguish between these possibilities.

While lung and liver metastasis formation were dependent on GSH synthesis, the formation of peritoneal metastases (PMs) was not. Although PMs are considered "distant" metastases, the metastatic route that underlies their initiation is essentially different from that of liver and lung metastases. When primary tumors have invaded and breached the intestinal wall, they gain direct access to the peritoneal cavity. Detached tumor cell clusters form the seeds for PM without the need for systemic spread.[49] This limits the generation of oxidative stress[16] and thus the necessity to cope with such stress. The different anatomical routes of dissemination and the distinct requirements for a single cell stage are likely to underlie the differential requirement for GSH synthesis during liver and lung versus PM formation. The differential requirement for GSH synthesis between distinct metastatic sites is therefore another important aspect of metastatic organotropism.[43,50]

Limitations of the study

Our study has identified BRAF^{V600E}-induced GCLC expression as a tumor-cell-intrinsic metastasis-facilitating mechanism, allowing tumor cells to withstand metastasis-associated redox stress. However, the *in vivo* studies were performed in immune-deficient mice, precluding the analysis of a potential role for immune cells. Further studies are therefore needed to assess if/how genetic or pharmacological modulation of the GSH system alters the immune microenvironment and the generation of anti-tumor immunity and how this affects metastatic capacity.

The altered redox state in cancer cells forms an intrinsic generic vulnerability that may be exploited with oxidative-stress-inducing drugs, such as the combination of BSO and auranofin.[32,51–53] Unfortunately, the clinical development of BSO has been discontinued due to its short half-life and inability to significantly reduce GSH levels in human tumors.[54] Moreover, we have found that treatment of tumor-bearing mice with auranofin and BSO produced very serious kidney toxicity, hampering the further preclinical development of this specific drug combination. An interesting alternative drug for targeting the GSH pathway is APR-246,[55] which is currently being tested in clinical trials. Moreover, several clinical trials testing auranofin in patients with cancer are currently ongoing but in the absence of GSH pathway inhibition. Our study shows that effective redox-based treatment of BRAF^{V600E} CRC is possible but requires simultaneous inhibition of BRAF—lowering the reductive capacity of these tumors—and inhibition of both the GSH and TRX pathway in order to induce lethal levels of oxidative stress. The potential nephrotoxicity of redox-based treatment strategies is a point of concern during further (pre-)clinical development.

STAR★METHODS

Detailed methods are provided in the online version of this paper and include the following:

- KEY RESOURCES TABLE
- RESOURCE AVAILABILITY
  - Lead contact
  - Materials availability
  - Data and code availability
- EXPERIMENTAL MODEL AND SUBJECT DETAILS
  - CRC patient-derived organoid (PDO) cultures
  - Multi-organ metastasis and subcutaneous mouse models
- METHOD DETAILS
  - *In vitro* drug screen
  - Comparative RNA sequencing analysis
  - Generation of lentiviral gRNAs constructs
  - Lentiviral production and PDO transduction
  - Antibodies and reagents
  - Immunohistochemistry and image data acquisition
  - IHC evaluation of staining of TMA

Figure 6. Expression of GCLC and BRAF^{V600E} reduce sensitivity to redox-targeting therapy

(A) Heatmap showing the sensitivity of 3 independent BRAF^{V600E} PDOs to auranofin treatment alone or in combination with increasing concentrations of BSO (0–200 μM; 72 h). Data are expressed as IC50 values.

(B) Heatmap showing the cell viability (percentage of control) of the same PDOs as in (A) after single-drug treatment with BSO (0–200 μM; 72 h).

(C) Dose-response curves of control (Ecas) and 3 independent GCLC-KO clones (1.6; 1.12, and 2.24) to increasing concentrations of auranofin (72 h). Data are presented as means ± SEM and are representative of three biological replicates. Each dot represents the mean of three technical replicates of each experiment.

(D) As in (C) but using 2 independent GCLM-KO clones (1 and 2). Data are presented as means ± SEM and are representative of three biological replicates. Each dot represents the mean of three technical replicates of each experiment.

(E) Heatmap showing the calculated IC50 values of single-drug auranofin treatment of all Tor10 variants tested as in (C) and (D).

(F) Immunoblot analysis of GCLC and β-actin expression levels in Laemmli lysates derived from Tor26T PDOs transduced with the empty lentiviral vector or with lentiviral vectors encoding FLAG-tagged or GFP-tagged GCLC.

(G) Tor26-EV-, FLAG-, or GFP-GCLC-overexpressing Tor26 PDO variants as in (F) were treated for 72 h with auranofin alone or in combination with increasing concentrations of BSO ranging from 2.5 to 10 μM. Graph showing ATP levels as a proxy for the amount of live cells (percentage of control). Data are presented as means ± SEM and are representative of three biological replicates; each dot represents the mean of three technical replicates of each experiment.

(H) Representative images of Tor20 PDOs transduced with the lentiviral FG12-GFP EV or with FG12-GFP-BRAF^{V600E} treated for 72 h with DMSO or with auranofin/BSO combination treatment. Scale bars, 100 μm.

(I) Dose-response curves of Tor20-EV or TOR20-BRAF^{V600E} to increasing concentrations of auranofin alone or in combination with 20 μM BSO (72 h). Data are presented as means ± SEM and are representative of two biological replicates; each dot represents the mean of three technical replicates of each experiment.

(J) Bar plots showing viability of Tor20-EV or TOR20-BRAF^{V600E} following exposure to increasing concentrations of BSO (5, 10, and 20 μM) (72 h) in the absence or presence of auranofin (1 μM). Data are presented as means ± SEM and are representative of two biological replicates; each dot represents the mean of three technical replicates of each experiment.

(K-M) As in (H)–(J) for Tor18T. Scale bars, 100 μm. Data are presented as means ± SEM and are representative of two biological replicates; each dot represents the mean of three technical replicates of each experiment (see also Figure S7).

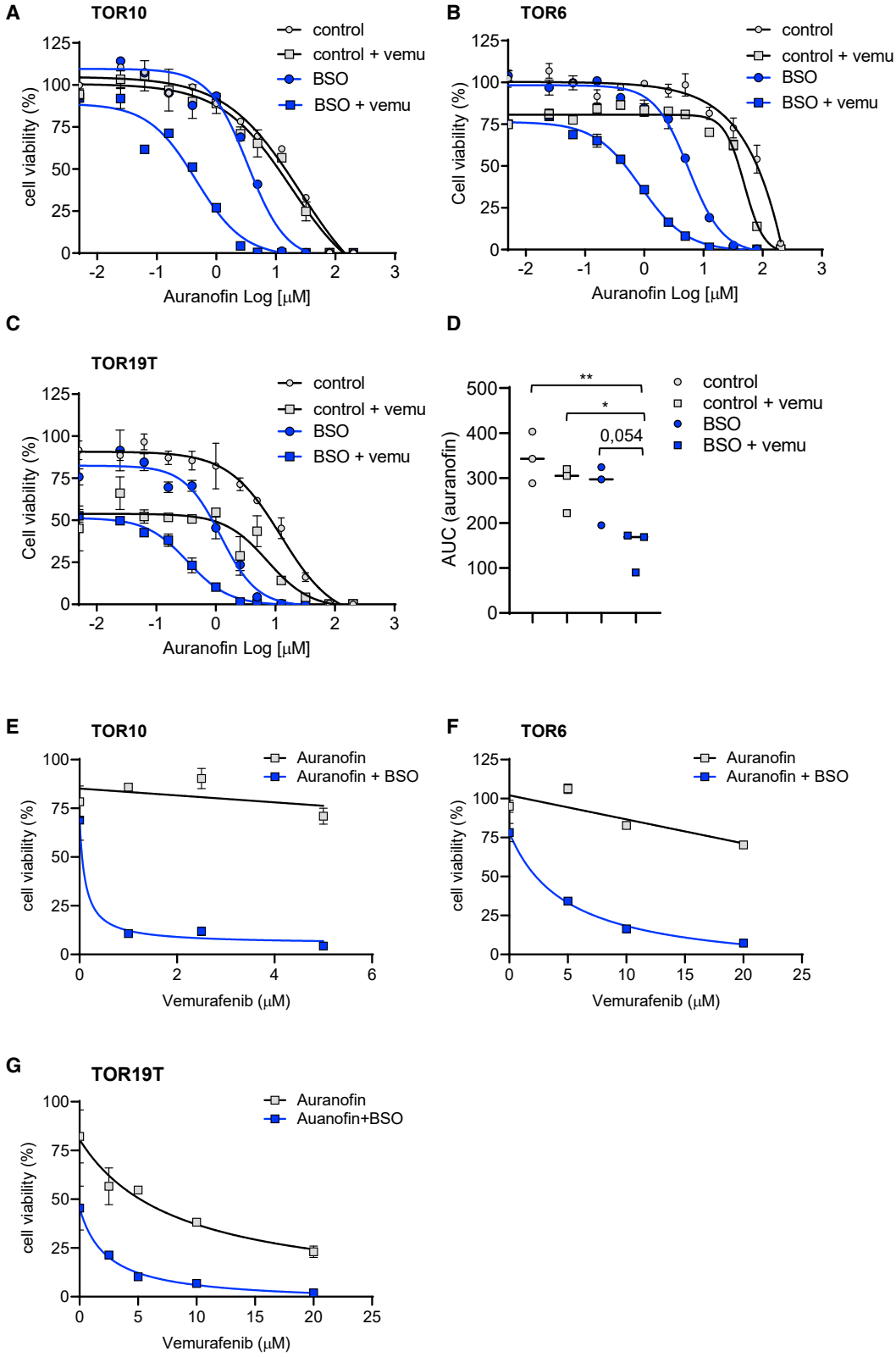

(legend on next page)

- GSH and H2O2 measurement
- Colony forming assay
- Western blot analysis

- QUANTIFICATION AND STATISTICAL ANALYSIS

SUPPLEMENTAL INFORMATION

Supplemental information can be found online at https://doi.org/10.1016/j.celrep.2022.111728.

ACKNOWLEDGMENTS

The authors thank Dr. Inge Ubink and Dr. Marc van de Wetering for PDO cultures and D. Raats and L. Wijler for help with setting up high-throughput drug screening. We also thank Miangela Lacle for help in scoring the CRC TMAs. This work was supported by grants from the Dutch Cancer Society (KWF-UMCU-8088 and UMCU-10660).

AUTHOR CONTRIBUTIONS

Study design, J.L. and O.K.; experimental work, J.L., S.v.S., E.K., A.V.; CAIRO TMA, genetic and clinical information, K.G. and M.K.; data interpretation, J.L., S.v.S., and O.K.; study supervision, I.B.R. and O.K.; manuscript writing, J.L. and O.K.

DECLARATION OF INTERESTS

The authors declare no competing interests.

Received: June 22, 2022
Revised: August 8, 2022
Accepted: November 3, 2022
Published: November 29, 2022

REFERENCES

1. Punt, C.J.A., Koopman, M., and Vermeulen, L. (2017). From tumour heterogeneity to advances in precision treatment of colorectal cancer. Nat. Rev. Clin. Oncol. *14*, 235–246. https://doi.org/10.1038/nrclinonc.2016.171.
2. Arnold, M., Sierra, M.S., Laversanne, M., Soerjomataram, I., Jemal, A., and Bray, F. (2017). Global patterns and trends in colorectal cancer incidence and mortality. Gut *66*, 683–691. https://doi.org/10.1136/gutjnl-2015-310912.
3. Michaloglou, C., Vredeveld, L.C.W., Mooi, W.J., and Peeper, D.S. (2008). BRAF(E600) in benign and malignant human tumours. Oncogene *27*, 877–895.
4. Safaee Ardekani, G., Jafarnejad, S.M., Tan, L., Saeedi, A., and Li, G. (2012). The prognostic value of BRAF mutation in colorectal cancer and melanoma: a systematic review and meta-analysis. PLoS One *7*, e47054. https://doi.org/10.1371/journal.pone.0047054.
5. Yaeger, R., Kotani, D., Mondaca, S., Parikh, A.R., Bando, H., Van Seventer, E.E., Taniguchi, H., Zhao, H., Thant, C.N., de Stanchina, E., et al. (2019). Response to anti-EGFR therapy in patients with BRAF non-V600-mutant metastatic colorectal cancer. Clin. Cancer Res. *25*, 7089–7097. https://doi.org/10.1158/1078-0432.CCR-19-2004.
6. Schirripa, M., Biason, P., Lonardi, S., Pella, N., Pino, M.S., Urbano, F., Antoniotti, C., Cremolini, C., Corallo, S., Pietrantonio, F., et al. (2019). Class 1, 2, and 3 BRAF-mutated metastatic colorectal cancer: a detailed clinical, pathologic, and molecular characterization. Clin. Cancer Res. *25*, 3954–3961. https://doi.org/10.1158/1078-0432.CCR-19-0311.
7. Jones, J.C., Renfro, L.A., Al-Shamsi, H.O., Schrock, A.B., Rankin, A., Zhang, B.Y., Kasi, P.M., Voss, J.S., Leal, A.D., Sun, J., et al. (2017). Non-V600) BRAF mutations define a clinically distinct molecular subtype of metastatic colorectal cancer. J. Clin. Oncol. *35*, 2624–2630. https://doi.org/10.1200/JCO.2016.71.4394.
8. Rodriquenz, M.G., Ciardiello, D., Latiano, T.P., Maiorano, B.A., Martinelli, E., Silvestris, N., Ciardiello, F., and Maiello, E. (2022). Exploring biological heterogeneity and implications on novel treatment paradigm in BRAF-mutant metastatic colorectal cancer. Crit. Rev. Oncol. Hematol. *173*, 103657. https://doi.org/10.1016/j.critrevonc.2022.103657.
9. Post, J.B., Roodhart, J.M.L., and Snippert, H.J.G. (2020). Colorectal cancer modeling with organoids: discriminating between oncogenic RAS and BRAF variants. Trends Cancer *6*, 111–129. https://doi.org/10.1016/j.trecan.2019.12.005.
10. Arnandis, T., Monteiro, P., Adams, S.D., Bridgeman, V.L., Rajeeve, V., Gadaleta, E., Marzec, J., Chelala, C., Malanchi, I., Cutillas, P.R., and Godinho, S.A. (2018). Oxidative stress in cells with extra centrosomes drives non-cell-autonomous invasion. Dev. Cell *47*, 409–424.e9. https://doi.org/10.1016/j.devcel.2018.10.026.
11. Ishikawa, K., Takenaga, K., Akimoto, M., Koshikawa, N., Yamaguchi, A., Imanishi, H., Nakada, K., Honma, Y., and Hayashi, J.I. (2008). ROS-generating mitochondrial DNA mutations can regulate tumor cell metastasis. Science *320*, 661–664. https://doi.org/10.1126/science.1156906.
12. O'Leary, B.R., Fath, M.A., Bellizzi, A.M., Hrabe, J.E., Button, A.M., Allen, B.G., Case, A.J., Altekruse, S., Wagner, B.A., Buettner, G.R., et al. (2015). Loss of SOD3 (EcSOD) expression promotes an aggressive phenotype in human pancreatic ductal adenocarcinoma. Clin. Cancer Res. *21*, 1741–1751. https://doi.org/10.1158/1078-0432.CCR-14-1959.
13. Porporato, P.E., Payen, V.L., Pérez-Escuredo, J., De Saedeleer, C.J., Danhier, P., Copetti, T., Dhup, S., Tardy, M., Vazeille, T., Bouzin, C., et al. (2014). A mitochondrial switch promotes tumor metastasis. Cell Rep. *8*, 754–766. https://doi.org/10.1016/j.celrep.2014.06.043.
14. Radisky, D.C., Levy, D.D., Littlepage, L.E., Liu, H., Nelson, C.M., Fata, J.E., Leake, D., Godden, E.L., Albertson, D.G., Nieto, M.A., et al. (2005). Rac1b and reactive oxygen species mediate MMP-3-induced EMT and genomic instability. Nature *436*, 123–127. https://doi.org/10.1038/nature03688.
15. Labuschagne, C.F., Cheung, E.C., Blagih, J., Domart, M.C., and Vousden, K.H. (2019). Cell clustering promotes a metabolic switch that supports metastatic colonization. Cell Metab. *30*, 720–734.e5. https://doi.org/10.1016/j.cmet.2019.07.014.
16. Padmanaban, V., Krol, I., Suhail, Y., Szczerba, B.M., Aceto, N., Bader, J.S., and Ewald, A.J. (2019). E-cadherin is required for metastasis in multiple models of breast cancer. Nature *573*, 439–444. https://doi.org/10.1038/s41586-019-1526-3.
17. Schafer, Z.T., Grassian, A.R., Song, L., Jiang, Z., Gerhart-Hines, Z., Irie, H.Y., Gao, S., Puigserver, P., and Brugge, J.S. (2009). Antioxidant and

Figure 7. Inhibition of BRAF^{V600E} sensitizes CRC PDOs to redox-targeting therapy

(A–C) Dose-response curves of mutant BRAF Tor10 (A), Tor6 (B), and Tor19T (C) PDOs to increasing concentrations of auranofin (72 h) alone or in combination with BSO (20 μM) in the absence or presence of vemurafenib (5 μM). All data are presented as means ± SEM and are representative of three biological replicates; each dot represents the mean of three technical replicates of each experiment.

(D) Graph showing area under the curve (AUC) in mutant BRAF Tor10, Tor6, and Tor19T PDOs based on the dose-response curves in (A)–(C). Significant differences between groups were determined by unpaired Student's t tests (*$p < 0.05$, **$p < 0.01$).

(E–G) Dose-response curves of mutant BRAF Tor10 (E), Tor6 (F), and Tor19T (G) PDOs to increasing concentrations of vemurafenib (72 h) in the absence or presence of auranofin (1.5 μM) and BSO (20 μM). All data are presented as means ± SEM and are representative of three biological replicates; each dot represents the mean of three technical replicates of each experiment (see also Figure S7).

oncogene rescue of metabolic defects caused by loss of matrix attachment. Nature *461*, 109–113. https://doi.org/10.1038/nature08268.

18. Emmink, B.L., Laoukili, J., Kipp, A.P., Koster, J., Govaert, K.M., Fatrai, S., Verheem, A., Steller, E.J.A., Brigelius-Flohé, R., Jimenez, C.R., et al. (2014). GPx2 suppression of H2O2 stress links the formation of differentiated tumor mass to metastatic capacity in colorectal cancer. Cancer Res. *74*, 6717–6730. https://doi.org/10.1158/0008-5472.CAN-14-1645.
19. Le Gal, K., Ibrahim, M.X., Wiel, C., Sayin, V.I., Akula, M.K., Karlsson, C., Dalin, M.G., Akyürek, L.M., Lindahl, P., Nilsson, J., and Bergo, M.O. (2015). Antioxidants can increase melanoma metastasis in mice. Sci. Transl. Med. *7*, 308re308. https://doi.org/10.1126/scitranslmed.aad3740.
20. Lignitto, L., LeBoeuf, S.E., Homer, H., Jiang, S., Askenazi, M., Karakousi, T.R., Pass, H.I., Bhutkar, A.J., Tsirigos, A., Ueberheide, B., et al. (2019). Nrf2 activation promotes lung cancer metastasis by inhibiting the degradation of Bach1. Cell *178*, 316–329.e18. https://doi.org/10.1016/j.cell.2019.06.003.
21. Nguyen, A., Loo, J.M., Mital, R., Weinberg, E.M., Man, F.Y., Zeng, Z., Paty, P.B., Saltz, L., Janjigian, Y.Y., de Stanchina, E., and Tavazoie, S.F. (2016). PKLR promotes colorectal cancer liver colonization through induction of glutathione synthesis. J. Clin. Invest. *126*, 681–694. https://doi.org/10.1172/JCI83587.
22. Piskounova, E., Agathocleous, M., Murphy, M.M., Hu, Z., Huddlestun, S.E., Zhao, Z., Leitch, A.M., Johnson, T.M., DeBerardinis, R.J., and Morrison, S.J. (2015). Oxidative stress inhibits distant metastasis by human melanoma cells. Nature *527*, 186–191. https://doi.org/10.1038/nature15726.
23. Sayin, V.I., Ibrahim, M.X., Larsson, E., Nilsson, J.A., Lindahl, P., and Bergo, M.O. (2014). Antioxidants accelerate lung cancer progression in mice. Sci. Transl. Med. *6*, 221ra15. https://doi.org/10.1126/scitranslmed.3007653.
24. Wiel, C., Le Gal, K., Ibrahim, M.X., Jahangir, C.A., Kashif, M., Yao, H., Ziegler, D.V., Xu, X., Ghosh, T., Mondal, T., et al. (2019). BACH1 stabilization by antioxidants stimulates lung cancer metastasis. Cell *178*, 330–345.e22. https://doi.org/10.1016/j.cell.2019.06.005.
25. Lu, S.C. (2013). Glutathione synthesis. Biochim. Biophys. Acta *1830*, 3143–3153. https://doi.org/10.1016/j.bbagen.2012.09.008.
26. Simkens, L.H.J., van Tinteren, H., May, A., ten Tije, A.J., Creemers, G.J.M., Loosveld, O.J.L., de Jongh, F.E., Erdkamp, F.L.G., Erjavec, Z., van der Torren, A.M.E., et al. (2015). Maintenance treatment with capecitabine and bevacizumab in metastatic colorectal cancer (CAIRO3): a phase 3 randomised controlled trial of the Dutch Colorectal Cancer Group. Lancet *385*, 1843–1852. https://doi.org/10.1016/S0140-6736(14)62004-3.
27. Goey, K.K.H., Elias, S.G., van Tinteren, H., Laclé, M.M., Willems, S.M., Offerhaus, G.J.A., de Leng, W.W.J., Strengman, E., Ten Tije, A.J., Creemers, G.J.M., et al. (2017). Maintenance treatment with capecitabine and bevacizumab versus observation in metastatic colorectal cancer: updated results and molecular subgroup analyses of the phase 3 CAIRO3 study. Ann. Oncol. *28*, 2128–2134. https://doi.org/10.1093/annonc/mdx322.
28. Fumagalli, A., Suijkerbuijk, S.J.E., Begthel, H., Beerling, E., Oost, K.C., Snippert, H.J., van Rheenen, J., and Drost, J. (2018). A surgical orthotopic organoid transplantation approach in mice to visualize and study colorectal cancer progression. Nat. Protoc. *13*, 235–247. https://doi.org/10.1038/nprot.2017.137.
29. Bylsma, L.C., Gillezeau, C., Garawin, T.A., Kelsh, M.A., Fryzek, J.P., Sangaré, L., and Lowe, K.A. (2020). Prevalence of RAS and BRAF mutations in metastatic colorectal cancer patients by tumor sidedness: a systematic review and meta-analysis. Cancer Med. *9*, 1044–1057. https://doi.org/10.1002/cam4.2747.
30. Zafarullah, M., Li, W.Q., Sylvester, J., and Ahmad, M. (2003). Molecular mechanisms of N-acetylcysteine actions. Cell. Mol. Life Sci. *60*, 6–20. https://doi.org/10.1007/s000180300001.
31. Fath, M.A., Ahmad, I.M., Smith, C.J., Spence, J., and Spitz, D.R. (2011). Enhancement of carboplatin-mediated lung cancer cell killing by simultaneous disruption of glutathione and thioredoxin metabolism. Clin. Cancer Res. *17*, 6206–6217. https://doi.org/10.1158/1078-0432.CCR-11-0736.
32. Harris, I.S., Treloar, A.E., Inoue, S., Sasaki, M., Gorrini, C., Lee, K.C., Yung, K.Y., Brenner, D., Knobbe-Thomsen, C.B., Cox, M.A., et al. (2015). Glutathione and thioredoxin antioxidant pathways synergize to drive cancer initiation and progression. Cancer Cell *27*, 211–222. https://doi.org/10.1016/j.ccell.2014.11.019.
33. Kiebala, M., Skalska, J., Casulo, C., Brookes, P.S., Peterson, D.R., Hilchey, S.P., Dai, Y., Grant, S., Maggirwar, S.B., and Bernstein, S.H. (2015). Dual targeting of the thioredoxin and glutathione antioxidant systems in malignant B cells: a novel synergistic therapeutic approach. Exp. Hematol. *43*, 89–99. https://doi.org/10.1016/j.exphem.2014.10.004.
34. Jin, Z., and Sinicrope, F.A. (2019). Advances in the therapy of BRAF(V600E) metastatic colorectal cancer. Expert Rev. Anticancer Ther. *19*, 823–829. https://doi.org/10.1080/14737140.2019.1661778.
35. Maughan, T.S., Adams, R.A., Smith, C.G., Meade, A.M., Seymour, M.T., Wilson, R.H., Idziaszczyk, S., Harris, R., Fisher, D., Kenny, S.L., et al. (2011). Addition of cetuximab to oxaliplatin-based first-line combination chemotherapy for treatment of advanced colorectal cancer: results of the randomised phase 3 MRC COIN trial. Lancet *377*, 2103–2114. https://doi.org/10.1016/S0140-6736(11)60613-2.
36. Stintzing, S., Miller-Phillips, L., Modest, D.P., Fischer von Weikersthal, L., Decker, T., Kiani, A., Vehling-Kaiser, U., Al-Batran, S.E., Heintges, T., Kahl, C., et al. (2017). Impact of BRAF and RAS mutations on first-line efficacy of FOLFIRI plus cetuximab versus FOLFIRI plus bevacizumab: analysis of the FIRE-3 (AIO KRK-0306) study. Eur. J. Cancer *79*, 50–60. https://doi.org/10.1016/j.ejca.2017.03.023.
37. Tran, B., Kopetz, S., Tie, J., Gibbs, P., Jiang, Z.Q., Lieu, C.H., Agarwal, A., Maru, D.M., Sieber, O., and Desai, J. (2011). Impact of BRAF mutation and microsatellite instability on the pattern of metastatic spread and prognosis in metastatic colorectal cancer. Cancer *117*, 4623–4632. https://doi.org/10.1002/cncr.26086.
38. Solit, D.B., Garraway, L.A., Pratilas, C.A., Sawai, A., Getz, G., Basso, A., Ye, Q., Lobo, J.M., She, Y., Osman, I., et al. (2006). BRAF mutation predicts sensitivity to MEK inhibition. Nature *439*, 358–362.
39. Loo, J.M., Scherl, A., Nguyen, A., Man, F.Y., Weinberg, E., Zeng, Z., Saltz, L., Paty, P.B., and Tavazoie, S.F. (2015). Extracellular metabolic energetics can promote cancer progression. Cell *160*, 393–406. https://doi.org/10.1016/j.cell.2014.12.018.
40. Fuhrmann, D.C., and Brüne, B. (2017). Mitochondrial composition and function under the control of hypoxia. Redox Biol. *12*, 208–215. https://doi.org/10.1016/j.redox.2017.02.012.
41. Rouschop, K.M., Dubois, L.J., Keulers, T.G., van den Beucken, T., Lambin, P., Bussink, J., van der Kogel, A.J., Koritzinsky, M., and Wouters, B.G. (2013). PERK/eIF2alpha signaling protects therapy resistant hypoxic cells through induction of glutathione synthesis and protection against ROS. Proc. Natl. Acad. Sci. USA *110*, 4622–4627. https://doi.org/10.1073/pnas.1210633110.
42. van der Waals, L.M., Jongen, J.M.J., Elias, S.G., Veremiyenko, K., Trumpi, K., Trinh, A., Laoukili, J., Ubink, I., Schenning-van Schelven, S.J., van Diest, P.J., et al. (2018). Increased levels of oxidative damage in liver metastases compared with corresponding primary colorectal tumors: association with molecular subtype and prior treatment. Am. J. Pathol. *188*, 2369–2377. https://doi.org/10.1016/j.ajpath.2018.06.008.
43. Schild, T., Low, V., Blenis, J., and Gomes, A.P. (2018). Unique metabolic adaptations dictate distal organ-specific metastatic colonization. Cancer Cell *33*, 347–354. https://doi.org/10.1016/j.ccell.2018.02.001.
44. Valavanidis, A., Vlachogianni, T., Fiotakis, K., and Loridas, S. (2013). Pulmonary oxidative stress, inflammation and cancer: respirable particulate matter, fibrous dusts and ozone as major causes of lung carcinogenesis through reactive oxygen species mechanisms. Int. J. Environ. Res. Public Health *10*, 3886–3907. https://doi.org/10.3390/ijerph10093886.
45. St-Pierre, J., Drori, S., Uldry, M., Silvaggi, J.M., Rhee, J., Jäger, S., Handschin, C., Zheng, K., Lin, J., Yang, W., et al. (2006). Suppression of reactive oxygen species and neurodegeneration by the PGC-1 transcriptional coactivators. Cell *127*, 397–408. https://doi.org/10.1016/j.cell.2006.09.024.

46. LeBleu, V.S., O'Connell, J.T., Gonzalez Herrera, K.N., Wikman, H., Pantel, K., Haigis, M.C., de Carvalho, F.M., Damascena, A., Domingos Chinen, L.T., Rocha, R.M., et al. (2014). PGC-1alpha mediates mitochondrial biogenesis and oxidative phosphorylation in cancer cells to promote metastasis. Nat. Cell Biol. *16*, 992–1003. https://doi.org/10.1038/ncb3039.

47. Stresing, V., Baltziskueta, E., Rubio, N., Blanco, J., Arriba, M.C., Valls, J., Janier, M., Clézardin, P., Sanz-Pamplona, R., Nieva, C., et al. (2013). Peroxiredoxin 2 specifically regulates the oxidative and metabolic stress response of human metastatic breast cancer cells in lungs. Oncogene *32*, 724–735. https://doi.org/10.1038/onc.2012.93.

48. Breau, M., Houssaini, A., Lipskaia, L., Abid, S., Born, E., Marcos, E., Czibik, G., Attwe, A., Beaulieu, D., Palazzo, A., et al. (2019). The antioxidant N-acetylcysteine protects from lung emphysema but induces lung adenocarcinoma in mice. JCI Insight *4*, 127647. https://doi.org/10.1172/jci.insight.127647.

49. Zajac, O., Raingeaud, J., Libanje, F., Lefebvre, C., Sabino, D., Martins, I., Roy, P., Benatar, C., Canet-Jourdan, C., Azorin, P., et al. (2018). Tumour spheres with inverted polarity drive the formation of peritoneal metastases in patients with hypermethylated colorectal carcinomas. Nat. Cell Biol. *20*, 296–306. https://doi.org/10.1038/s41556-017-0027-6.

50. Gao, Y., Bado, I., Wang, H., Zhang, W., Rosen, J.M., and Zhang, X.H.F. (2019). Metastasis organotropism: redefining the congenial soil. Dev. Cell *49*, 375–391. https://doi.org/10.1016/j.devcel.2019.04.012.

51. Benhar, M., Shytaj, I.L., Stamler, J.S., and Savarino, A. (2016). Dual targeting of the thioredoxin and glutathione systems in cancer and HIV. J. Clin. Invest. *126*, 1630–1639. https://doi.org/10.1172/JCI85339.

52. Trachootham, D., Alexandre, J., and Huang, P. (2009). Targeting cancer cells by ROS-mediated mechanisms: a radical therapeutic approach? Nat. Rev. Drug Discov. *8*, 579–591. https://doi.org/10.1038/nrd2803.

53. Trachootham, D., Zhou, Y., Zhang, H., Demizu, Y., Chen, Z., Pelicano, H., Chiao, P.J., Achanta, G., Arlinghaus, R.B., Liu, J., and Huang, P. (2006). Selective killing of oncogenically transformed cells through a ROS-mediated mechanism by beta-phenylethyl isothiocyanate. Cancer Cell *10*, 241–252. https://doi.org/10.1016/j.ccr.2006.08.009.

54. Kirkpatrick, D.L., and Powis, G. (2017). Clinically evaluated cancer drugs inhibiting redox signaling. Antioxid. Redox Signal. *26*, 262–273. https://doi.org/10.1089/ars.2016.6633.

55. Ogiwara, H., Takahashi, K., Sasaki, M., Kuroda, T., Yoshida, H., Watanabe, R., Maruyama, A., Makinoshima, H., Chiwaki, F., Sasaki, H., et al. (2019). Targeting the vulnerability of glutathione metabolism in ARID1A-deficient cancers. Cancer Cell *35*, 177–190.e8. https://doi.org/10.1016/j.ccell.2018.12.009.

56. van de Wetering, M., Francies, H.E., Francis, J.M., Bounova, G., Iorio, F., Pronk, A., van Houdt, W., van Gorp, J., Taylor-Weiner, A., Kester, L., et al. (2015). Prospective derivation of a living organoid biobank of colorectal cancer patients. Cell *161*, 933–945. https://doi.org/10.1016/j.cell.2015.03.053.

57. Ubink, I., Bolhaqueiro, A.C.F., Elias, S.G., Raats, D.A.E., Constantinides, A., Peters, N.A., Wassenaar, E.C.E., de Hingh, I.H.J.T., Rovers, K.P., van Grevenstein, W.M.U., et al. (2019). Organoids from colorectal peritoneal metastases as a platform for improving hyperthermic intraperitoneal chemotherapy. Br. J. Surg. *106*, 1404–1414. https://doi.org/10.1002/bjs.11206.

58. Koopman, M., Antonini, N.F., Douma, J., Wals, J., Honkoop, A.H., Erdkamp, F.L., de Jong, R.S., Rodenburg, C.J., Vreugdenhil, G., Loosveld, O.J., et al. (2007). Sequential versus combination chemotherapy with capecitabine, irinotecan, and oxaliplatin in advanced colorectal cancer (CAIRO): a phase III randomised controlled trial. Lancet *370*, 135–142.

59. Sanjana, N.E., Shalem, O., and Zhang, F. (2014). Improved vectors and genome-wide libraries for CRISPR screening. Nat. Methods *11*, 783–784. https://doi.org/10.1038/nmeth.3047.

STAR★METHODS

KEY RESOURCES TABLE

REAGENT or RESOURCE	SOURCE	IDENTIFIER
Antibodies		
Ki67	Novocastra	NCL-Ki67p; RRID:AB_442102
GCLC (IHC)	Atlas	HPA036359; RRID:AB_10672243
PanCK	ThermoFisher	MA5-13156; RRID:AB_10983023
yH2AX	ThermoFisher	MA5-27753; RRID:AB_2735313
hNuc	Abcam	ab190710
Cleaved-Caspase3	Cell Signaling	#9661; RRID:AB_2341188
GSH	Abcam	ab19534; RRID:AB_880243
MAPK p44/42 (Erk1/2) phospho (Thr202/Tyr204)	Cell Signaling	#9101; RRID:AB_331646
MEK1/2 phospho(Ser217/221)	Cell Signaling	#9121; RRID:AB_331648
MAPK p44/42 (Erk1/2) (137F5)	Cell Signaling	#4695; RRID:AB_390779
GCLC antibody [EP13475] (Western-Blot)	Abcam	ab190685; RRID:AB_2889925
GCLM	Abcam	ab126704; RRID:AB_11127439
Glutathione Synthetase (GS)	Abcam	ab124811; RRID:AB_10973222
Thioredoxin Reductase 1 (TXNRD1)	Abcam	ab124811; RRID:AB_10975643
NrF2 phospho (pS40) mAb	ABGent	AJ1555b; RRID:AB_10817040
GPX2	Gift from Pr. Dr. Anna Kipp	N/A
b-Actin AC15	Novus	NB600-501; RRID:AB_10077656
Bacterial and virus strains		
Stbl3™ E. coli strain	ThermoFisher	C737303
Biological samples		
CRC Patient-Derived Organoids (PDOs)	van de Wetering et al.[56]; Ubink et al.[57]	HUB-Cancer TcBio#12–09
Tissue Microarray (TMA) of primary CRC tumors (CAIRO3)	Koopman et al.[58]	N/A
Chemicals, peptides, and recombinant proteins		
L-Buthionine-sulfoximine (BSO)	Santa Cruz	sc-218630A
Auranofin	Santa Cruz	sc-202476
Vemurafenib (PLX4032)	Selleckchem	S1267
N-Acetyl-L-cysteine (NAC)	Sigma	A9165
Y-27632 (ROCK inhibitor)	Abmole bioscience	HY-10583
Eosine	Klinipath	4082–9002
Haematoxyline Mayer	Merck	1.092.492.500
dispase II	Roche	12273600
TrypLE™ Express Enzyme	ThermoFisher	12604013
Matrigel matrix	Corning	354234
BME	Amsbio	3533-010-02
Critical commercial assays		
CellTiter-Glo 3-D	Promega	G9681
GSH-Glo™	Promega	V6911
Amplex-Red	Invitrogen	A12222
RNeasy® Mini Kit	Qiagen	74004
Truseq RNA stranded poly A Library Preparation Kit	Illumina	20020594
Deposited data		
RNA sequencing Raw and Analyzed Data	This paper	http://r2.amc.nl (Table S2)
RNA sequencing Raw Data	This paper	GEO repository (GSE213896)

(*Continued on next page*)

Continued

REAGENT or RESOURCE	SOURCE	IDENTIFIER
Experimental models: Cell lines		
CRC Patient-Derived Organoids (PDOs)	van de Wetering et al.[56]; Ubink et al.[57]	HUB-Cancer TcBio#12–09
Experimental models: Organisms/strains		
NOD.Cg-Prkdcscid Il2rgtm1Wjl/SzJ NSG® Mouse	Distributed by Charles River Laboratories; https://www.jax.org/strain/005557	Strain # 005557
Oligonucleotides		
gRNA-hGCLC-Oligo1-Forward 5′CACC GGCACATCTACCACGCCGTCA	This paper	N/A
gRNA-hGCLC-Oligo1-Reverse 5′ AAAC TGACGGCGTGGTAGATGTGCC	This paper	N/A
gRNA-hGCLC-Oligo2-Forward 5′CACC GTGTGCCGGTCCTTGACGGCG	This paper	N/A
gRNA-hGCLC-Oligo2-Reverse 5′ AAAC CGCCGTCAAGGACCGGCACAC	This paper	N/A
gRNA-hGCLM-Oligo1-Forward 5′CACC GGTGCCCGTCCACGCACAGCG	This paper	N/A
gRNA-hGCLM-Oligo1-Reverse 5′ AAAC CGCTGTGCGTGGACGGGCACC	This paper	N/A
gRNA-hGCLM-Oligo2-Forward 5′CACC GTGGACGGGCACTTCTTCCGC	This paper	N/A
gRNA-hGCLM-Oligo2-Reverse 5′ AAAC GCGGAAGAAGTGCCCGTCCAC	This paper	N/A
Recombinant DNA		
lentiCRISPR v2		Addgene #52961
psPAX2 50661	Didier Trono	Addgene #12260
pMD2.G	Didier Trono	Addgene #12259
pLV-Lucif-IRES-GFP	Gift from Dr. Patrick Derksen	N/A
FG12-CMV-Lenti-GFP	Gift from Pr. Dr. Daniel Peeper	N/A
FG12-CMV-Lenti-GFP-BRAFV600E	Gift from Pr. Dr. Daniel Peeper	N/A
lentiCRISPR v2-GCLC1	This paper	N/A
lentiCRISPR v2-GCLC2	This paper	N/A
lentiCRISPR v2-GCLM1	This paper	N/A
lentiCRISPR v2-GCLM2	This paper	N/A
Software and algorithms		
GraphPad Prism 8	GraphPad	https://www.graphpad.com/scientific-software/prism/
ImageJ	ImageJ	https://imagej.nih.gov/ij/
QuPath	QuPath	https://qupath.github.io/
R2 Genomics Analysis and Visualization Platform	R2	http://r2.amc.nl
Other		
RNA sequencing and Data analysis	This paper	www.USEQ.nl www.UBEC.nl

RESOURCE AVAILABILITY

Lead contact

Further information and requests for resources and reagents should be directed to and will be fulfilled by the lead contact, Onno Kranenburg (o.kranenburg@umcutrecht.nl).

Materials availability

Plasmids generated in this study are available from the lead contact. PDOs may be obtained from the lead contact with a completed materials transfer agreement.

Data and code availability

- All data reported in this paper will be shared by the lead contact upon request. The RNA-sequencing data of the isolated tumors derived from Hub98 and Tor1 PDO mouse models were deposited to GEO repository with accession number (GSE213896).
- This paper does not report original code.
- Any additional information required to reanalyze the data reported in this paper is available from the lead contact upon request.

EXPERIMENTAL MODEL AND SUBJECT DETAILS

CRC patient-derived organoid (PDO) cultures

CRC PDOs used in this study were either previously established and characterized or newly established from tumor specimens.[57,56] Human CRC tumor specimens were obtained from patients undergoing a colon or liver resection for respectively primary or metastatic adenocarcinoma, or were collected during cytoreductive surgery (CRS) or diagnostic laparoscopy for peritoneal metastasis (PM). All tumor samples were collected within biobanking protocol HUB-Cancer TcBio#12-09, which was approved by the medical ethics committee of the University Medical Center Utrecht. Informed consent was obtained from all patients. See Table S1 for an overview of all PDOs used in this study including their clinical parameters and mutational status.

For passaging, PDOs were washed once with PBS and were subsequently dissociated using TrypLE express (Invitrogen) for 5–10 min at 37°C to obtain single cells. Cells were then washed with PBS and resuspended in CRC growth medium (see Table S4) containing advanced DMEM/F12 (Invitrogen) supplemented with B27 serum (Invitrogen), with HEPES buffer (Lonza, 10 mM), penicillin/streptomycin (Gibco, 50 U/mL), GlutaMAX (Gibco, 2 mM), 20% R-spondin conditioned medium, 10% Noggin conditioned medium, N-Acetyl Cysteine (Sigma-Aldrich, 0,5–1 mM), A83-01 (SignalChem, 500 nM), SB202190 (Gentaur, 10 μM), human recombinant EGF (Sigma, 50ng/mL) and Primocin (Invitrogen, 100 μg/mL). Cells were subsequently plated as droplets of Basement Membrane Extract (BME; Amsbio) or Matrigel (BD Biosciences) at a 1:3 ratio.

Multi-organ metastasis and subcutaneous mouse models

Pathogen-free, 8–9-week-old male NOD.Cg-Prkdcscid Il2rgtm1Wjl/SzJ/J (NGS) weighing between 20 and 25g were purchased from Charles River. Upon arrival into the animal facility, mice were quarantined for 2 weeks for acclimatization. All mice used in experiments throughout the study exhibited normal health, were housed in groups of 4–5, and randomly assigned for the experimental groups. For spontaneous metastatic capacity of the tumor PDOs, we made use of the murine orthotopic caecum-implantation model.[28] In summary, PDOs expressing Luciferase-GFP were dissociated using TrypLE for 5–10 min at 37°C to obtain single cells. Cells were then washed with medium and plated in neutralized Rat Tail High Concentrated Type I Collagen (Corning) to obtain 2,5 × 10^5 cells in 6–10ul organoid droplets and were allowed to recover overnight at 37°C, 5% (vol/vol) CO2. 30 min before surgery, mice were treated with a subcutaneous dose of Carprofen (5 mg/kg, RimadylTM) and were subsequently sedated by using isoflurane inhalation anesthesia [∼2% (vol/vol) isoflurane/O2 mixture]. The caecum was exteriorized through a midline abdominal incision and a single collagen droplet containing the PDOs was micro-surgically transplanted into the submucosa of the caecum wall. Carprofen was given 24h post-surgery. After 12–16 weeks mice were sacrificed and tumor load was assessed using BLI and immunohistochemical analysis.

For subcutaneous injections we used the equivalent of 5 × 10^5 cells mixed with Matrigel (BD Biosciences) at a 1:1 ratio (total volume 100μL) and injected subcutaneously into the right flank of 8–9 weeks old male NGS mice. Tumor growth and volume were evaluated once a week using BLI and Caliper measurements respectively. When the tumor size reached approximatively 1 cm^3, mice were sacrificed and tumors were processed either for BLI or immunohistochemistry analysis. All studies involving laboratory animals were approved by Utrecht University's Animal Welfare Body, the Animal Ethics Committee and licensed by the Central Authority for Scientific Procedures on Animals (license number AVD115002016614). All experiments were conducted in accordance with the Dutch Experiments on Animals Act, in line with European Directive 2010/63/EU and by licensed personnel.

METHOD DETAILS

In vitro drug screen

PDOs were washed once with PBS, dissociated into single cells using TrypLE, washed in PBS, resuspended in CRC growth medium and plated in BME matrix. 2 to 5 days old organoids (depending on the CRC organoid line) were released from the BME matrix by addition of 1 mg/mL dispase II (Invitrogen) to the medium of the organoids and incubation for 30–45 min at 37°C. Organoids were subsequently washed with PBS, counted and re-suspended in Reduced organoid medium containing basal DMEM-F12 growth medium supplemented with B27 serum (Invitrogen), HEPES buffer (Lonza, 10 mM), penicillin/streptomycin (Gibco, 50 U/mL), and

GlutaMAX (Gibco, 2 mM). The equivalent of 1000 organoids in a 30 μL volume were then plated on 10ul BME pre-coated 384-well plates using Multi-drop Combi Reagent Dispenser. The drugs and their combinations were added 3 h after plating the organoids using the Tecan D300e Digital Dispenser. All wells were normalized for solvent used. DMSO percentage or aqueous solution/Tween 20 never exceeded 1%, or 5% respectively. Drug exposure was performed in triplicate for each concentration shown. Auranofin, and Vemurafenib were dissolved in DMSO. BSO was dissolved in water/0.3% Tween 20. Cell viability was measured 48–72h after drug exposure using the CellTiter-Glo 3-D Reagent (Promega, catalog no. G9681) according to the manufacturer's instructions, and luminescence was measured using SpectraMax M5 microplate reader (Molecular Devices).

Comparative RNA sequencing analysis

PDOs TOR1 and TOR98 were transplanted into the caecum of NSG mice as above (n = 4), or were injected subcutaneously (n = 4). Subcutaneous tumors, primary caecum tumors, peritoneal metastases and either lung metastases (TOR1) or liver metastases (TOR98) were harvested and snap frozen. Frozen tissue samples were cut into 20–30-μm thick cryosections with a cryostat and immersed in RLT buffer (RNeasy® Mini Kit; Qiagen, Stockholm, Sweden) plus 1 per cent β-mercaptoethanol. RNA isolation, including on-column DNase digestion, was performed according to the manufacturer's instructions. RNA concentration was measured using a NanoDrop™ 2000 instrument (Thermo Fisher Scientific). Samples with RNA integrity (RIN) values below 8 were excluded from further analysis. In total we analyzed 4 samples from each site. Generation of sequencing libraries was performed using the Truseq RNA stranded poly A Library Preparation Kit (Illumina, San Diego, CA, USA). Sequencing was performed on Illumina NextSeq500 with 75-bp reads (Illumina). The RNAseq dataset was uploaded into R2 (http://r2.amc.nl) for subsequent bioinformatics analyses and is available on the platform. Differential gene expression analysis was performed between primary tumor samples and liver metastases (TOR98) or primary tumor samples and lung metastases (TOR1), using a cut off of $p < 0.01$ (ANOVA) with multiple testing correction by false discovery rate. This was followed by analysis of the enrichment of all KEGG pathways (n = 551) in the resulting gene lists.

Expression of the 'glutathione metabolism' pathway was determined by using the 'view gene set' option and storing the resulting meta-gene values. The relate-two-tracks option was used to compare expression of this gene set in samples grouped by tissue-origin.

Generation of lentiviral gRNAs constructs

CRISPR guide RNAs (sgRNAs) targeting human GCLC or human GCLM genes were generated using plenti-CrisprV2-Ecas vector (Addgene, #52961) as described by.[59] Briefly, 4 independent GCLC or GCLM gRNAs were annealed and subsequently ligated to the plenti-CrisprV2-Ecas vector cut with BsmBI, and sequence verified. The GCLC and GCLM target sequences used were respectively:

gRNA-hGCLC-Oligo1-Forward: 5′CACC GGCACATCTACCACGCCGTCA
gRNA-hGCLC-Oligo1-Reverse: 5′ AAAC TGACGGCGTGGTAGATGTGCC
gRNA-hGCLC-Oligo2-Forward: 5′CACC GTGTGCCGGTCCTTGACGGCG
gRNA-hGCLC-Oligo2-Reverse: 5′ AAAC CGCCGTCAAGGACCGGCACAC
gRNA-hGCLM-Oligo1-Forward: 5′CACC GGTGCCCGTCCACGCACAGCG
gRNA-hGCLM-Oligo1-Reverse: 5′ AAAC CGCTGTGCGTGGACGGGCACC
gRNA-hGCLM-Oligo2-Forward: 5′CACC GTGGACGGGCACTTCTTCCGC
gRNA-hGCLM-Oligo2-Reverse: 5′ AAAC GCGGAAGAAGTGCCCGTCCAC.

Lentiviral production and PDO transduction

Lentiviral production was performed using a calcium phosphate transfection protocol in human embryonic kidney 293T cells using the transfer plasmid (15 μg), pMD2.G (Addgene, #12259, 7.5 μg) and psPAX2 (Addgene, #12260, 7.5 μg). The following day, medium was replaced by advanced DMEM/F12 medium (Invitrogen) supplemented with HEPES buffer (Lonza, 10 mM), penicillin/streptomycin (Gibco, 50 U/mL), and GlutaMAX (Gibco, 2 mM). For lentiviral virus transduction, PDOs were dissociated using TrypLE and incubated for over-night with lentivirus medium (which was filtered through a 0.45 μm polyethersulfone filter), supplemented with Polybrene (Sigma-Aldrich, 8 μg/mL), N-acetylcysteine (Sigma-Aldrich, 1.25mM) and ROCK-inhibitor Y-27632 (Sigma-Aldrich, 10 μM), and incubated overnight 37°C, 5% (vol/vol) CO2 on non-adherent plates (ultra-low attachment surface, Sigma-Aldrich). After 24h incubation, cells were washed twice in PBS (Sigma-Aldrich), plated in matrigel and cultured as described above. For PDO transduced with plenti-CrisprV2, subsequent selection by adding 1ug/mL of puromycin to the culture medium was performed as described. To track tumor and metastasis formation *in vivo*, organoids were subsequently transduced with lentivirus encoding luciferase linked to GFP gene (pLV-Lucif-IRES-GFP).

FG12-CMV-Lenti-GFP and FG12-CMV-Lenti-GFP-BRAFV600E were kindly provided by Pr. Dr. Daniel Peeper (Netherlands Cancer Institute).

Antibodies and reagents

Table S5 gives an overview of the list of antibodies and experimental conditions used in the current study. L-Buthionine-sulfoximine (BSO) and Auranofin were purchased from Santa Cruz. N-Acetyl-L-cysteine (NAC) was purchased from Sigma-Aldrich. Vemurafenib (PLX4032) was purchased from selleckchem.

Immunohistochemistry and image data acquisition

Immunohistochemical (IHC) stainings were performed on 4-μm serial sections of paraformaldehyde fixed, paraffin-embedded tumors. The sections were incubated with antibodies recognizing GCLC (Sigma-Aldrich), pan-cytokeratin, Ki67, phosphorylated histone H2AX (gH2AX). Table S5 gives an overview of antibodies and dilutions, incubation conditions, and antigen-retrieval methods for each marker. For all stainings, sections were deparaffinized with xylene and rehydrated with serial dilutions of ethanol and water. Next, endogenous peroxidase activity was blocked with 1.5% hydrogen peroxide diluted in phosphate-buffered saline. Quantification of staining was performed using Qu-Path program analysis program.

IHC slides were scanned using NanoZoomerXR whole slide scanner (Hamamatsu) at 40× magnification, with a resolution of 0.25 μm/pixel. Quantification of the scans was performed using QuPath program analysis program.

Analysis of Pan-cytokeratin (PanCK) positive tumor area: PanCK positive tumor area (percent tumor area per liver or lung area) in three serial H&E-stained sections was quantified using QuPath's Trained Pixel classification command that allows an automated recognition of background, tissue (hematoxylin) and DAB (panCK) staining areas. Manual outlining of each panCK positive tumor region as well as total tissue area was subsequently performed, and annotated. The percentage of PanCK positive tumor area was then measured by using the following formula: (Total extracted background Tumor area)/(Total extracted background tissue area)x100.

Analysis of Ki67 and γH2AX IHC: Analysis of the number of Ki67 and gH2AX positive tumor cells was performed using QuPath's Positive Cell detection command. This command estimates staining intensity for hematoxylin and DAB, and cells are classified as positive or negative based upon a single intensity threshold (0,2 or 0,25) applied to the mean nuclear DAB optical density within the specified tumor regions. This protocol provides the percentage of total nuclei as well as the percentage of positive nuclei within the tumor area.

IHC evaluation of staining of TMA

A 0.6-mm (triple-core) tissue microarray (TMA) of primary CRC tumors (CAIRO3) was used.[58] For immunohistochemical staining, multiple serial sections (4 mm thick) were cut and stained for pan-cytokeratin and GCLC.

Scoring was performed by consensus of two investigators (J.L. and S.V.S) blinded to clinicopathological data and after training by a pathologist (Miangela Lacle). Damaged and empty TMA cores and those not containing cancer cells were excluded. For GCLC staining, intensity was scored as 0 (negative), 1 (weak), 2 (moderate), or 3 (strong).

GSH and H2O2 measurement

GSH concentrations were measured using the GSH-Glo assay (Promega) according to the manufacturer's instructions. H2O2 concentrations were measured using Amplex-Red (Invitrogen) kit following the manufacturer's instructions.

Colony forming assay

Organoids were dissociated using TrypLE and filtered through a 40-μm pore size nylon cell strainer (BD Falcon), and counted. Single cells were then suspended in BME matrix and plated at 500 cells in 25μL BME 50% v/v solution per 12-well. After polarization of the BME at 37C, the wells were filled with reduced basal DMEM/F12 medium containing B27 serum (Invitrogen), HEPES buffer (Lonza, 10 mM), penicillin/streptomycin (Gibco, 50 U/mL), and GlutaMAX (Gibco, 2 mM), in the absence or presence of BSO supplemented with or without 1mM N-Acetyl Cysteine (NAC). The medium was refreshed twice a week. The number of colonies were counted after 2 weeks of culturing using an inverted microscope (Nikon Eclipse TS100).

Western blot analysis

Organoid cultures were harvested at the indicated time points using dispase, washed with PBS and lysed in Laemmli lysis buffer (2.5% SDS, 20% glycerol, 120 mM TRIS pH6.8). Equal amounts of protein (10–20 μg) were run on SDS-PAA gels transferred onto nitrocellulose membranes (Trans-Blot Turbo, Bio-Rad, Hercules, CA, USA), and incubated with antibodies as described. Primary antibodies to TXNRD1, GCLC, GCLM, and Glutathione Syntehase (GS) were all purchased from Abcam. GPX2 antibody was a (Kind gift from Anna Kipp (Friedrich Schiller University Jena, FSU. Institute of Nutrition, Germany). Phospho-Mek1/2, phospho-Erk1/2 (Thr202/Tyr204) and phospho-AKT (Ser473) (163H12) were all from Cell Signaling. Phospho-NRF2 phospho (pS40) mAb was purchased from (ABGent), p53 antibody (Santa Cruz antibodies), and b-actin (Novus). Table S5 gives an overview of antibodies and dilutions.

QUANTIFICATION AND STATISTICAL ANALYSIS

For statistical analyses, we used GraphPad Prism software (version 8) for Windows (GraphPad Software, La Jolla, CA). Unpaired Student's t test was used for all histological analyses. One-way ANOVA was used for KEGG glutathione metabolism gene signature analysis. Values are presented as means ± SEM. A value of $p < 0.05$ was considered significant. For *in vivo* work, n = number of individual animals. Details regarding statistical tests, n values and p values can be found in the Figure Legends. Further details regarding the quantification methods used for IHC experiment are provided in the method details.